Design and testing of aeroelastically tailored composite wing under fatigue and gust loading including effect of fatigue on aeroelastic performance

Rajpal, D.; Mitrotta, F.M.A.; Socci, C. A.; Sodja, J.; Kassapoglou, C.; De Breuker, R.

DOI
10.1016/j.compstruct.2021.114373

Publication date
2021

Document Version
Final published version

Published in
Composite Structures

Composite Structures 275 (2021) 114373

Contents lists available at ScienceDirect

Composite Structures

journal homepage: www.elsevier.com/locate/compstruct

Design and testing of aeroelastically tailored composite wing under fatigue and gust loading including effect of fatigue on aeroelastic performance

D. Rajpal, F.M.A. Mitrotta, C.A. Socci, J. Sodja, C. Kassapoglou *, R. De Breuker *

Section of Aerospace Structures and Computational Mechanics, Faculty of Aerospace Engineering, Delft University of Technology, Kluyverweg 1, 2629 HS Delft, The Netherlands

ARTICLE INFO

Keywords:
Experimental aeroelasticity
Structural optimization
Fatigue
Gust loads
Composite wing

ABSTRACT

The aim of the paper is to experimentally validate a numerical design methodology for optimizing composite wings subject to gust and fatigue loading requirements and to assess the effect of fatigue on the aeroelastic performance of the wing. Traditionally, to account for fatigue in composite design, a knockdown factor on the maximum stress allowable is applied, resulting in a conservative design. In the current design methodology, an analytical fatigue model is used to reduce the conservativeness and exploit the potential of composite materials. To validate the proposed analytical model, a rectangular composite wing is designed and manufactured to be critical in strength, buckling and fatigue. An experimental campaign comprising wind tunnel and fatigue tests is performed. In the wind tunnel, both static and dynamic aeroelastic experiments are conducted to validate the numerical dynamic aeroelastic model. The fatigue test is used to validate the analytical fatigue model and to understand the effect of fatigue on aeroelastic properties of the wings. The results from experimental campaign validated both the aeroelastic predictions as well as fatigue predictions of the numerical design methodology. However the fatigue process resulted in degradation of the wing stiffness leading to change in the aeroelastic response of the wing.

1. Introduction

Composite materials with their high specific strength are becoming a preferred choice for an efficient aircraft structure. Additionally due to the inherent anisotropic behavior, composite materials can also be tailored to obtain higher efficiency during flight by achieving ideal aeroelastic deformations. There has been a lot of work on the application of composite materials to aeroelastically tailor the aircraft wings with an objective of minimizing the structural weight [1–6].

In a majority of these studies [1–7], the static maneuver load cases are used to size the structure with design constraints, among others on stiffness, buckling, static strength, control reversal and static and dynamic aeroelastic stability. As the wings become more optimized for improved aeroelastic behavior, unsteady gust loads start to size the structure along with the static load cases [8]. Taking into account gust loads during the initial phase of the design process is quite challenging as one has to scan approximately 10 million load cases to identify the worst-case gust load [9]. Additionally, after every iteration, there is an update in the design which changes the aeroelastic properties of the wing leading to a change in critical gust load. As a result, a rescan of all the load cases is required at every new iteration in the design. The authors [8] in their previous work have developed a methodology to include critical gust loads efficiently in the aeroelastic optimization of composite wings using the TU Delft in–house preliminary aeroelastic design tool PROTEUS [10].

Typically to account for fatigue in a composite structure, a conservative knockdown factor is applied to the allowable stress levels of the laminate. With improved aeroelastic behavior, the difference between the magnitude of typical fatigue loads and the ultimate static strength of the design becomes smaller. As a result, fatigue loading, which, historically, was not a design driver for a composite wing structure, now becomes more important and may impact the design. The conservative knockdown factors for fatigue would be too conservative and weight-inefficient. Thus there is a need to include fatigue through a physics-based model in the aeroelastic optimization process. The authors, in their previous work [11] formulated an analytical model to predict the fatigue life of composite structures. This model was integrated into PROTEUS to perform stiffness and thickness optimization of a composite wing taking into account fatigue as one of the constraints.

The present work aims at validating the numerical methodology developed to tailor composite wings subject to gust and fatigue loads by design, manufacturing and testing of a composite wing having a

* Corresponding authors at: Kluyverweg 1, 2629 HS Delft, The Netherlands.
E-mail addresses: c.kassapoglou@tudelft.nl (C. Kassapoglou), r.debreuker@tudelft.nl (R. De Breuker).

https://doi.org/10.1016/j.compstruct.2021.114373
Received 23 December 2020; Revised 4 June 2021; Accepted 13 July 2021
Available online 21 July 2021

representative wing structure comprising of spars, ribs and load bearing skins. Additionally, the work also looks at the effect of fatigue on the aeroelastic response of the wing. There is limited literature available on the aeroelastic experimental data sets of tailored composite wings. Early research has been focused on testing of wings modeled as plates [12–14] which are tailored to improve aeroelastic behavior using the bend-twist coupling of the composite laminate. However, for the representative wing structure, a closed-cell cross-sectional configuration is used where the improved aeroelastic behavior originates from the extension-shear coupling of the individual laminates of the cross-section. At the German Aerospace Center DLR, there has been a concentrated effort on optimization, manufacturing and testing of an aeroelastically tailored wing with representative cross section using composite materials [15–17]. In these studies, the wing is manufactured using load-carrying skins filled with foam. The foam is used to provide resistance against buckling. Ribs and spars are not included in the wing, in order to simplify the manufacturing.

More recently at Delft University of Technology TU Delft, Werter et al. [10] have manufactured and tested aeroelastically tailored wings having load-carrying skins filled with foam in the wind tunnel under static maneuver loadings. The designed wing employed constant thickness and stiffness along the span, such that a manufacturable stacking sequence could be obtained by a sweep over ply angles. Although the wings tested at DLR and TU Delft have tailored composite skins, they all feature foam as internal structure in place of spars and ribs. Thus, they are not entirely representative of a realistic wing as they miss the typical wingbox structure.

The current paper extends the work done by Werter et al. [10] by first designing and manufacturing a composite wing with an actual wing box, which includes ribs and spars such that there are clear load carrying paths; second, by testing under gust loading conditions, and third by performing fatigue tests on it. For this purpose, a carbon fiber rectangular wing is optimized subjected to static and gust loads, including the analytical fatigue model. The optimized wing is manufactured using unidirectional UD prepreg and undergoes an experimental test campaign comprising of following steps:

1. The pristine wing is tested in the low subsonic OJF [18] wind tunnel at the TU Delft under static and dynamic (gust) conditions. The data from this wind tunnel test is used to validate the numerical methodology of evaluating gust loads. The data will also be used to benchmark the performance of the pristine wing.
2. In the second step, using a MTS 100KN fatigue machine, the wing is fatigued to a predefined number of cycles that it is designed for. The data from the fatigue tests are used to validate the formulated analytical fatigue model.
3. The fatigued wing is finally tested again in the wind tunnel under static and gust conditions. With this test, the effect of fatigue on the aeroelastic response of the wing is analyzed by comparing it to the response of the pristine wing measured in step 1.

The paper starts with giving an overview of the design methodology in Section 2, which is formulated to optimize a manufacturable and tailored composite wing. In Section 3, the optimization problem is introduced and the optimized design is explained. This is followed by Section 4, which explains the manufacturing process of the composite wing. The experimental setup is described in Section 5. Finally, the experimental results are analyzed in Section 6, followed by the conclusions in Section 7.

2. Design framework

To design and manufacture a composite wing optimized for gust loads and fatigue loads, a design framework is formulated, which includes, along with PROTEUS, OptiBLESS [19], an open-source stacking-sequence-retrieval algorithm, and a commercial software MSC Nastran [20].

As mentioned before, PROTEUS is an in-house preliminary aeroelastic tool developed at the Delft University of Technology. In PROTEUS, the three-dimensional wing shape is defined by the planform and the airfoil sections along the span. The structure which is represented by skins and spars is defined by means of distinct composite laminates. These laminates are described in terms of lamination parameters and laminate thickness, leading to a set of continuous design variables. Based on the laminate properties, a cross-sectional modeler, especially developed for anisotropic shells, converts the three dimensional structure of a wing into a Timoshenko stiffness matrix. The geometrically nonlinear Timoshenko beam model is then coupled to an unsteady vortex lattice aerodynamic model to carry out a nonlinear aeroelastic solution. On top of this nonlinear equilibrium solution, a linear dynamic aeroelastic analysis is performed. In the post-processing step, the strains in the three dimensional structure are retrieved using the cross-sectional modeler. These strains are then used to calculate the strength, buckling and fatigue properties of the wing. A detailed explanation of PROTEUS and the extension to account for gust and fatigue loads is given in the references [10,11,8].

OptiBLESS is an open-source toolbox used to retrieve blended and manufacturable stacking sequences from the lamination parameters optimized by PROTEUS. This toolbox employs a patch-based optimization strategy including blending to obtain a blendable stacking sequence from several sets of lamination parameters representing different neighboring laminates. In OptiBLESS, the stacking sequence is considered blended when the plies of the thinnest laminate patch span the entire structural component. A detailed explanation of the capabilities and the methodologies employed in OptiBLESS is given in [19].

MSC Nastran is a standard tool for aeroelastic computation within the aerospace industry. The reason for coupling the approach with a finite element software such as MSC Nastran is threefold.

- The first reason is to have a numerical model which includes the spar flanges, since these are not modeled in PROTEUS. This is necessary in order to verify that the flange is sufficiently strong to resist crippling.
- The second reason is the correction of conservative buckling calculations in PROTEUS, which is based on idealized buckling model derived by Dillinger [21]. Besides this, the presence of spar flange results in a stiffening effect on the wing structure, which reduces the strains in the laminates and thus needs to be accounted for in PROTEUS. By means of the higher fidelity model in Nastran, it is possible to assess the level of the conservativeness of PROTEUS analysis and apply a correction.
- Finally, using a finer mesh in MSC Nastran, a better approximation of the local stresses in the bonded spar flange and skin is obtained. The local stresses are needed to make sure the shear stress experienced by the spars, which will be transferred through the bond line, is lower than the shear strength of the adhesive bond itself.

A MATLAB routine is developed to translate the beam model from PROTEUS into a 2D shell model in MSC Nastran, making use of the wing geometry and of the laminates' properties. By combining MSC Nastran with PROTEUS, a multi fidelity design framework is formulated which optimizes the wing in a computationally efficient manner as compared to optimizing the wing only with MSC Nastran.

Fig. 1 shows the flow diagram of the design framework used to optimize the composite wing. The first step consists of defining the wing geometry, the load cases, the initial laminate distribution and pertinent material properties. Furthermore, an initial width is chosen for the flange, which is later used for the generation of the Nastran model of the wing. The flange width is constant along the span. Based

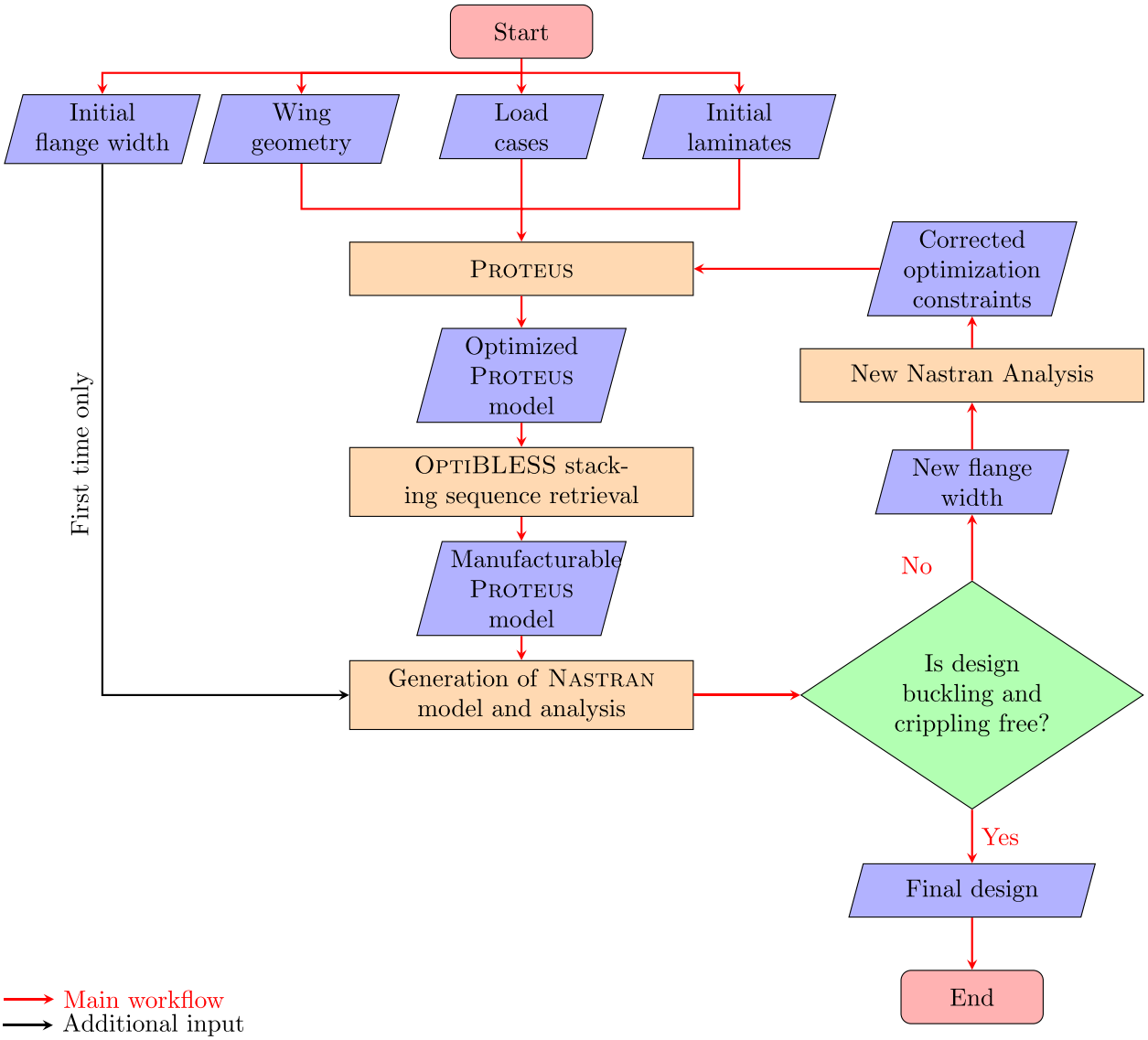

Fig. 1. Flow diagram of the design framework.

on the input variables, objective functions, design variables and constraints, stiffness and thickness optimization of the composite wing is performed within PROTEUS. This optimized design is fed to OptiBLESS, which transforms the results from the lamination parameter domain to the stacking sequence domain. After this operation, a manufacturable design in terms of feasible laminates is obtained. The new lamination parameters, associated with the stacking sequence found by OptiBLESS, are calculated and fed to PROTEUS, which analyzes the design to evaluate the incurred changes in the aeroelastic behavior. Following this step, the PROTEUS design is converted into a MSC Nastran aeroelastic model. For the first loop of the process, the model is evaluated with an initial flange width and the level of the conservativeness of PROTEUS is assessed so that the strain and buckling constraints can be corrected. From the second loop onward, a check is performed on the crippling load of the flange as defined in [22] and the maximum shear stress in the bond line. If the crippling load and maximum shear stress requirements are satisfied, the process is stopped; otherwise, a new flange size is selected and the optimization constraints are updated according to the new conservativeness assessment.

A more detailed analysis of the design framework is given in [23].

3. Optimization study

3.1. Optimization approach

Using the aforementioned framework, an aeroelastically tailored rectangular wing having a span of 1.75 m and a chord of 0.25 m is designed by taking into account gust and fatigue loading requirements. The wing geometrical parameters are summarized in Table 1. The

Table 1
Characteristics of the experimental composite wing.

Parameter	Value	Unit
Half Span	1.75	m
Leading edge sweep angle	0	degr
Front spar location	25	% chord
Rear spar location	65	% chord
Number of Ribs	13	% chord
Wing aspect ratio	14	–
Taper ratio	1	–
Wing chord	0.25	m
Airfoil	NACA 0010	–

wing has two spars located at 25% and 65% of the chord. The location of the rear spar is defined such as to guarantee a minimum web height of at least 15 mm. A total of 13 ribs is used, with spacing increasing from wing root to tip. The ribs at the root are clustered together as the skin panels are more prone to buckle. For the present case, the wing is divided into three design regions. An overview of the design regions, together with the layout of spars and ribs, is given in Fig. 2.

Table 2 shows the material properties used for the experimental wing. Knockdown factors of 0.65 and 0.80 are used to account for damage and environment, respectively, resulting in a net knockdown factor of 0.52 which is applied to the stress allowables. Table 3 gives the information regarding the optimization setup considered in the current study.

With a goal of obtaining a light and flexible wing, the objective of the optimization is set to maximize the wing tip deflection and minimize the wing weight. The laminates in the upper and lower skins and the front and the rear spars are optimized while the laminates in the ribs are pre-defined. The top and bottom skins of the wing are divided into three spanwise laminates, whereas the front and rear spars are represented by a single laminate each. This distribution results in eight unique laminates. Laminates are symmetric and allowed to be unbalanced. For every laminate, there are eight lamination parameters and one thickness variable resulting in a total number of 72 design variables. However, the thickness of the spars is set to be 0.524 mm, corresponding to four plies, which is not further optimized. This choice is made for ease of manufacturing and to reduce the complexity of the crippling assessment. Consequently, the number of active design variables is reduced to 70. The distribution of the laminates along the top skin is shown in Fig. 3. In the initial design, all the laminates are balanced and quasi-isotropic. In each of the laminates shown in Fig. 3, the stiffness distribution is depicted in terms of the polar plot of thickness normalized modulus of elasticity $\hat{\mathbf{E}}_{11}(\theta)$ which is given by

$$\hat{\mathbf{E}}_{11}(\theta) = \frac{1}{\hat{\mathbf{A}}_{11}^{-1}(\theta)} \tag{1}$$

where $\hat{\mathbf{A}}$ is the thickness normalized in-plane stiffness matrix and θ ranges from 0 to 360 degrees. With this stiffness distribution, a circle represents a quasi-isotropic laminate having equal stiffness in all directions, whereas a deformed plot represents a tailored stiffness distribution.

To ensure realistic ply distributions, Lamination feasibility equations formulated by Hammer et al. [24], Raju et al. [25] and Wu et al. [26] are applied. Failure envelope based on the Tsai-Wu criterion formulated for the lamination parameter domain by Khani et al. [27] is used to assess the static strength of the laminate. The stability of the panel in buckling is based on the idealized buckling model formulated by Dillinger et al. [3]. To make sure that the wing is aeroelastically stable, the real part of the eigenvalues of the state matrix should be less than zero.

The fatigue life of the laminate is calculated for the load spectrum, which is based on spectrum, which is based on a shortened version of the TWIST spectrumMini-TWIST [28]. The TWIST spectrum represents realistic loads experienced by the wing as it is based on load spectra obtained for a number of aircraft types covering a wide range of weights, gust loads, cruising speeds and design-flight distance. Table 4

Table 2
Material properties.

Property	Value
E_{11}	148.3 GPa
E_{22}	9.3 GPa
G_{12}	4.7 GPa
ν_{12}	0.32 –
ρ	1,570 kg/m^3
X_t	2,500 MPa
X_c	1,716 MPa
Y_t	64 MPa
Y_c	285.7 MPa
S	91.2 MPa

Table 3
Optimization setup.

Type	Parameter	# responses
Objective	Maximize wing tip deflection + Minimize wing weight	2
Design Variables	Lamination Parameter Laminate Thickness	70
Constraints	Laminate Feasibility Static Strength Buckling Fatigue Aeroelastic Stability	72 416/load case 768/load case 184 10/load case
Load cases	Static load case Dynamic load case	3 10

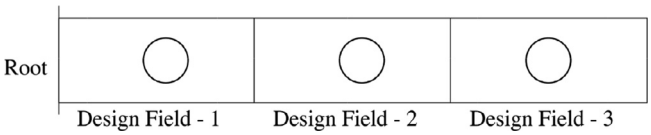

Fig. 3. Initial guess for laminate distribution of the top skin of experimental wing.

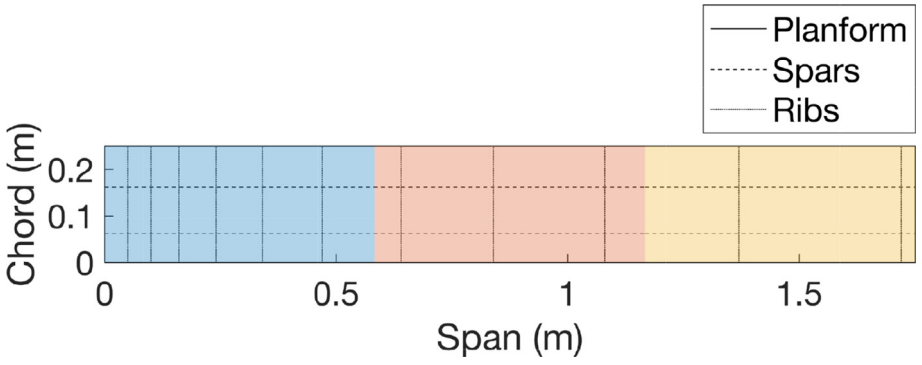

Fig. 2. Wing planform with layout of spars and ribs. The different colors indicate the design regions.

Table 4
Load spectrum used to evaluate fatigue.

Load level	Frequency per block	Number and magnitude of amplitude level												
		1	2	3	4	5	6	7	8	9	10	11	12	13
		3.08	2.97	2.82	2.69	2.56	2.3	1.78	0.97	0.69	0.56	0.29	0.22	0.17
		Number of Cycles per load type												
A	1	1	4	4	4	16	18	15	2	1	8	18	15	24
B	1		4	4	4	10	11	16	1	4	5	11	16	19
C	3			4	4	18	7	16	2	5	9	7	16	12
D	19				1	31	1	1	1	1	15	1	1	4
E	120					26	1	1			13	1	1	6
F	260						1	1					1	1
G	382							1					1	1
H	220							1					1	
Total Number of Cycles per block		1	8	20	39	3,789	449	1,080	28	39	1,885	449	1,080	1,517

depicts the load spectrum used to evaluate the fatigue of the designed composite wing. The spectrum consists of eight load levels where each level has thirteen different levels of stress ratio. The stress ratio has been normalized to the stress level at cruise condition. At each stress ratio, the number of cycles is different for different load levels. The eight levels are repeated based on the frequency, in a random manner to make a one block which is equal to 10,000 cycles. In reality, cycles with highest load levels occur randomly during the fatigue life and hence out of the eight levels in the spectrum, care needs to be taken that the first three levels having the highest stress ratio are not clustered together as they might have the highest effect on fatigue. The block of 10,000 cycles is repeated 10 times, to accumulate 100,000 cycles which is considered as the maximum life of the wing. For evaluating the fatigue life of the laminate, the loads obtained from the cruise load case are used as a mean load on top of which the fatigue spectrum is applied.

Table 5 gives the information on the load cases which are used for the current study. The first three load cases represent the static manoeuver load cases. The fourth load case is a gust load case where, for the given combination of velocity and angle of attack, ten gust gradients ranging from 2 m to 6 m were applied. These load cases represent the limit load, which is defined as the maximum load the wing is expected to experience in service. To satisfy the requirements for the ultimate load, an additional safety factor of 1.5 is applied to the strength and buckling values calculated for the limit loads.

3.2. Optimization results

The optimization with PROTEUS results in stiffness and thickness distribution shown in Fig. 4. The strain, buckling and fatigue factors of the optimized design are shown in Fig. 5 (where more than 1 denotes failure). The inner part of the top skin and the first rib bay of the second laminate for both top and bottom skin are dominated by buckling and fatigue. With respect to strains, only the middle part of the bottom skin of the wing adjacent to the ply drop between first and the second laminate is critical. Since the thickness at the transition point between the first and the second laminate of the bottom skin drops by 40%, this region is sensitive to buckling, fatigue and strain. Looking at the stiffness distribution in Fig. 4, the optimizer achieves the objective of maximizing the tip deflection by orienting the in-plane stiffness in all the laminates forward relative to the wing axis, resulting in reduced stiffness in the wing axis direction and thus maximizing the flexibility. For the laminates, which are critical in buckling, the out of plane stiffness is tailored as well.

OptiBLESS is then used to retrieve the blended stacking sequences from the lamination parameters optimized by PROTEUS. The resulting stacking sequences of top and bottom skins and the spars are given in Table 6. The front and rear spars have the same stacking sequence and since they are not critical for any constraints, they are not mentioned further in the current discussion. The use of OptiBLESS to retrieve blended stacking sequences inevitably affects the thickness and stiffness of the laminates. The effect can be observed in Fig. 6. The only laminate undergoing a change in laminate thickness smaller than 5% is the one corresponding to the first design region of the top skin. All the other laminates experience a 10 to 30 percent change in thickness, caused by the fact that the blended laminate thickness must be a multiple of the ply thickness. Moreover, it can be observed that, in most cases, the blended laminates are thinner than the optimal laminates. The reason for this is twofold. First, the result of the optimization performed in OptiBLESS is influenced by the bounds set in terms of number of plies. In the present case, the bounds are set such that manufacturable design is not conservative with respect to the PROTEUS result. Furthermore, the simultaneous symmetry and blending constraints on the laminates forces the OptiBLESS to remove an even number of plies at the ply drops. This leads to thinner laminates in the outboard region compared to PROTEUS result.

As far as the change in stiffness is concerned, Fig. 7 shows a comparison between the stiffness polars of the optimum and of the blended laminates. As already noticed with the stacking sequence table, the stiffness is mainly directed away from the span axis, both for the optimum and the blended laminates and especially considering the in-plane stiffness. However, substantial differences can be observed between the stiffness of the optimum and the blended laminates. Only the in-plane stiffnesses of the first design region of both skins are well matched and the quality of the match deteriorates progressively in the following design regions. This is the consequence of blending requirements combined with the relatively small number of available plies. In fact, the laminate of the first design region of each skin is the thickest and this gives to the optimizer used in OptiBLESS a design space large enough to match the optimum stiffness. However, when switching to

Table 5
List of static and gust load cases.

Load case ID	V_{EAS} (m/s)	Altitude (m)	Load Factor (–)	Angle of Attack (degrees)
1	28	0	1	3
2	28	0	2.5	7.5
3	28	0	−1	−3
4	28	0	1	3

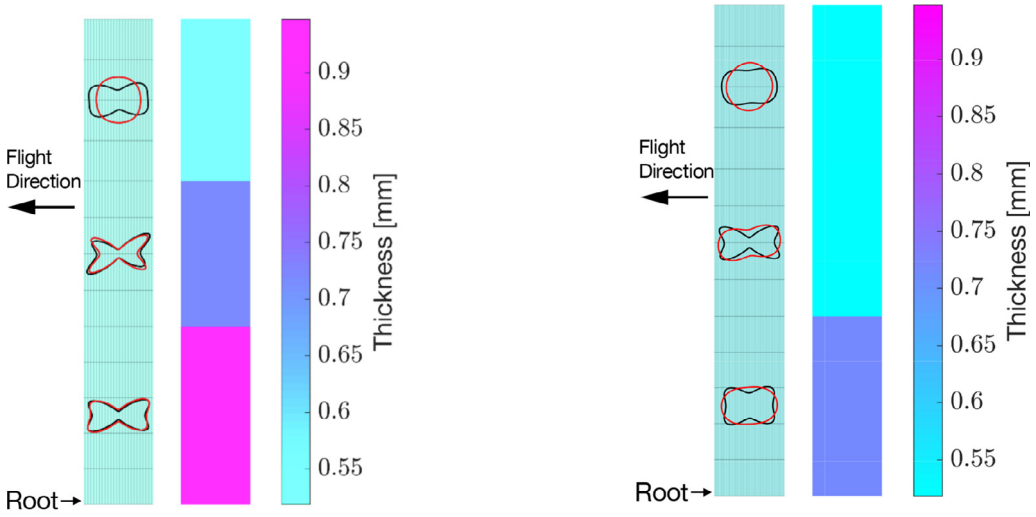

(a) Top Skin. (b) Bottom Skin.

Fig. 4. Stiffness and thickness distribution for the optimized wing (Black: In-plane stiffness, Red: Out-of-plane stiffness.). (For interpretation of the references to color in this figure legend, the reader is referred to the web version of this article.)

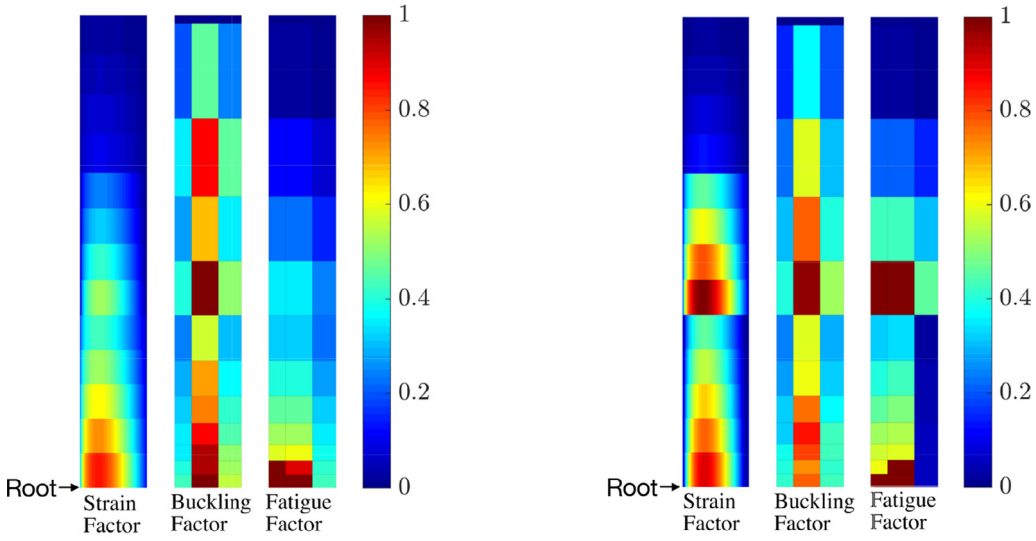

(a) Top Skin. (b) Bottom Skin.

Fig. 5. Strain and buckling factor distribution on the optimized wing.

Table 6
Stacking sequence table of top and bottom skins and spars, ply angles in degrees.

Top skin			Bottom skin			Spar		
Design region #			Design region #			Design region #		
1	2	3	1	2	3	1	2	3
55	55	55	−75	−75	−75	70	70	70
−65	−65		50			−60	−60	−60
75			−30			−60	−60	−60
−70	−70	−70	55	55	55	70	70	70
75			−30					
−65	−65		50					
55	55	55	−75	−75	−75			

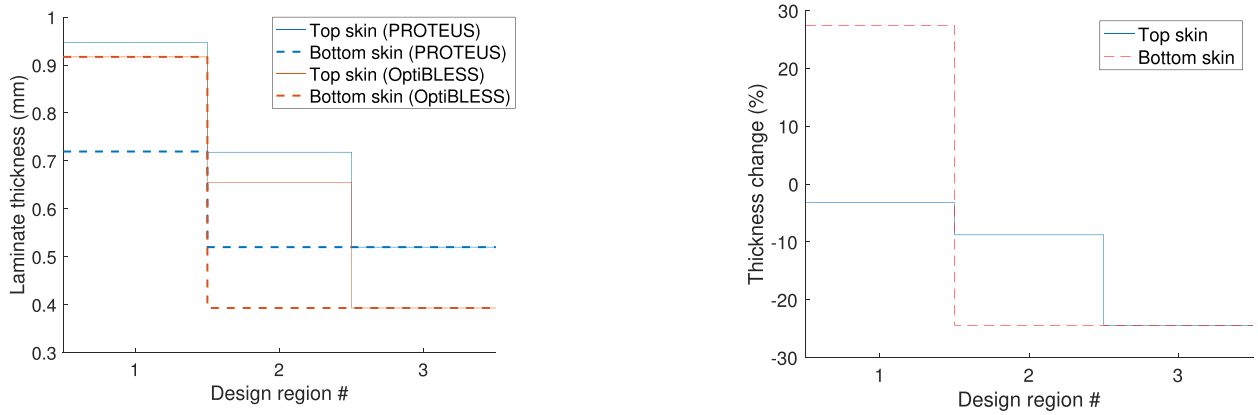

(a) Laminate thickness.

(b) Change in laminate thickness.

Fig. 6. Comparison between the thickness of non blended and blended laminates obtained from PROTEUS and OptiBLESS, respectively.

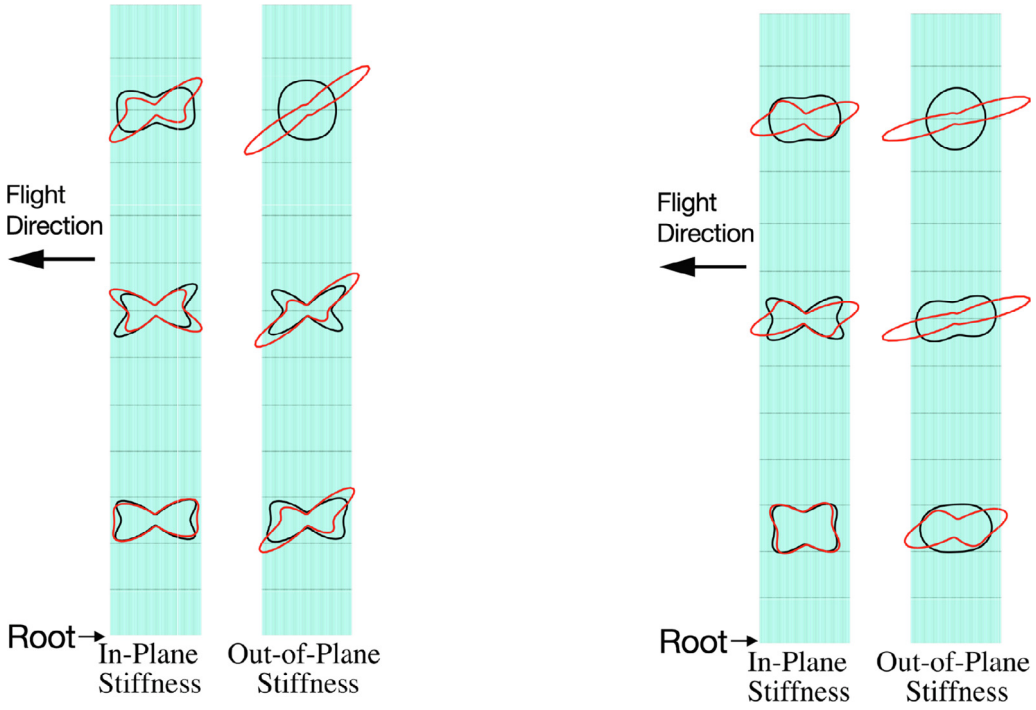

(a) Top Skin.

(b) Bottom Skin.

Fig. 7. Comparison between the stiffness polars of non blended and blended laminates obtained from PROTEUS and OptiBLESS respectively (Black: PROTEUS design, Red: OptiBLESS design.). (For interpretation of the references to color in this figure legend, the reader is referred to the web version of this article.)

the laminate of the adjacent patch, the design space is reduced both by the need to continue some plies from the previous patch and by the reduced number of plies. This makes the matching of both in-plane and out-of-plane stiffnesses over the entire skin very challenging.

4. Manufacturing

The optimized wing with a span of 1.8 m and a chord of 0.25 m is manufactured using a hand layup technique using IM7/8552 UD prepreg. The experimental wing is extended by 50 mm at the root with respect to the nominal span of 1.75 m. An aluminum block is inserted inside the first 50 mm of the wing-box section to facilitate the clamping mechanism of the wing. A female half mold is used to manufacture the skins and male mold is used to manufacture the spars. Both molds are milled out of aluminum. To connect the top and the bottom skins, a bridging strip called as Leading Edge Strip LE strip is also manufactured using a separate aluminum male mold. All the molds are designed with a tolerance of 0.5 mm. The ribs are cut from prefabricated 3 mm thick quasi-isotropic carbon fiber plates. All the components, namely: top skin, bottom skin, front spar, rear spar and the LE strip are cured individually and then bonded together using Araldite AW 4858. To monitor strains experienced by the wing, an optical strain fiber sensor is attached in a criss-cross pattern to the bottom skin of the wing using a super-glue. The advantage of such a strain fiber is the high resolution of the strains obtained along the length of the fiber. The optical fiber used for strain sensing in the current experiment is a 5 m long LUNA HD-FOS strain sensor. The sensor is based on Rayleigh backscattering.

The manufacturing procedure of building the composite wing is segmented into six main parts, starting with cutting of the necessary patches, laying-up of the patches in the mold followed by curing, trimming, surface preparation and finally bonding. The following steps give more insight into the steps involved in manufacturing of the composite wing.

- In the first step, the UD prepreg roll is cut into the individual patches having required dimensions and ply orientation using the GERBER laminate cutting machine at the Delft Aerospace Structures and Materials Laboratory DASML. The cutting bench, along with the prepreg roll, can be seen in Fig. 8a. Since the width of the roll, used to cut the patches, is 1200 mm, it is not possible to have single patches having a length of 1.75 m with fiber orientations larger than 40 degr. Therefore, for patches having fiber orientations larger than 40 degr, smaller sub-patches are joined by aligning them side by side along the fiber orientation to get a longer patch. Care is taken to make sure that no two such joints in adjacent plies lined up with each other in order to facilitate load transfer and minimize stress concentration effects. Fig. 8b shows the side view of the layup of the top skin where the dashed line indicates the region of the joined sub patches.

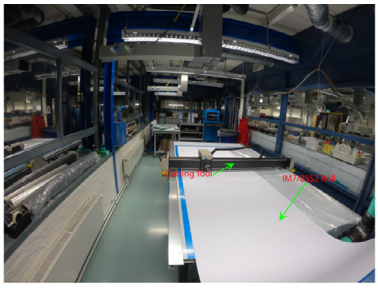

(a) The GERBER laminate cutting bench.

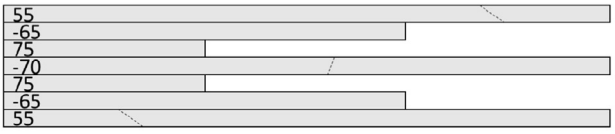

(b) Side view of the ply layup of the top skin (Text indicates the ply angle and the dashed line indicates the region of the joined sub-patches).

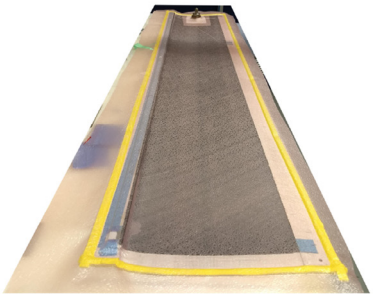

(c) Debulking of the top skin of the wing.

(d) Vacuum bagging of the top skin of the wing.

(e) Bonded skeleton consisting of spars and ribs.

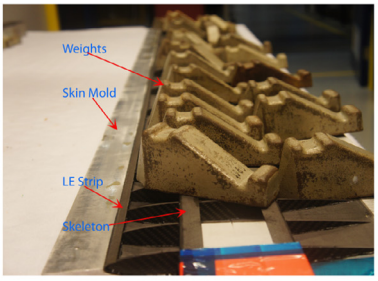

(f) Skeleton being bonded to the top skin of the wing.

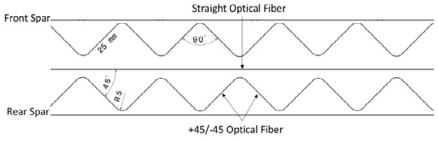

(g) Drawing of the fiber-pattern.

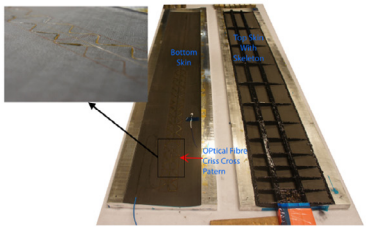

(h) Two halves of the wing before being closed.

Fig. 8. Manufacturing process.

- The trimmed patches are moved to the laminating clean-room facility at the DASML where the process of laying-up is performed. The patches are placed on the mold based on the stacking sequence of each part as detailed in Table 6. After every three layers, debulking of the stacked plies for around 5 min is done to consolidate the plies to the tooling and force out any trapped air caught between the individual layers. Once all the plies are layed up, the mold is covered with perforated foil to allow the excess resin to flow out. A breather material is put on top of the perforated foil and finally, a vacuum bag covers the entire part. Fig. 8c depicts the top skin being debulked after laying up the first three layers and Fig. 8d shows the top skin vacuum bagged just before putting it in the autoclave for curing.
- The vacuum bagged part is then cured in the autoclave. The cure process followed the cycle recommended by the material supplier which lasts approximately 6 hours.
- The cured skins, spars and the LE strip are trimmed into the right dimensions and the ribs are cut from the quasi-isotropic carbon fiber plates to the required dimensions using a CNC water-jet cutting machine.
- To achieve good adhesion and improve the durability of the bonded structures, the surface to be bonded is mechanically abraded using sandpaper and cleaned using acetone to remove any contaminations. A limited number of contact angle measurement tests (water break) is done to make sure the quality of the surface preparation is optimal for bonding.
- Once all the parts are trimmed and the surfaces are prepared for bonding, the bonding of the entire wing starts. Since there is a tolerance of 0.5 mm in the mold designs, a constant bond line thickness of 0.5 mm is targeted. Care is taken to avoid creation of bond-lines with varying thickness by uniformly spreading the adhesive paste along the bonded surface. In the bonding process, first, the front and the rear spars and the ribs are bonded using the aforementioned adhesive paste. Fig. 8e depicts the bonded skeleton of ribs and spars.
- Next, the top skin is placed in the mold and the skeleton is bonded to the top skin. The LE strip is also bonded to the top skin of the wing. Weights are placed on the skeleton to get a good bond between the spars, ribs and the skin. Fig. 8f shows the skeleton placed on the top skin. Additionally, a chemically etched aluminum block is also bonded to the root of the top skin. This block is later used to clamp the wing to the test setup.
- The optical strain fiber is then attached to the bottom skin of the wing using a super-glue. In the first half of the bottom skin, the fiber is layed out in a criss-cross pattern to get strains in 3 directions, which can then be later post-processed to get normal strains and shear strain. In the criss-cross pattern, the angle between the each segment is 90 degr and the length of each segment is 25 mm. The segments are oriented at 45 degr and −45 degr alternatively with respect to the span of the wing. The radius of the corner is 5 mm. Due to the constraint on the length of the fiber, in the second half of the wing, the fiber is layed out in a straight line along the span of the wing. The drawing of the fiber pattern is shown in Fig. 8g.
- Finally, the wing is closed by placing, the bottom skin with the fiber attached, on the top skin with the skeleton, and glued together with the adhesive paste. Care is taken to match a number of locations around the perimeter of upper and lower skin and that the upper skin is lowered uniformly to the lower one to avoid the creation of bond-lines with varying thickness. Fig. 8h shows the bottom skin with the attached fiber and the top skin with skeleton glued just before closing the wing.

5. Experimental setup

The aim of the experimental campaign is twofold.

1. The first one is to validate the numerical methodology of designing a composite wing with fatigue as an active constraint.
2. The second is to assess the effect of fatigue on the aeroelastic response of the wing.

For this purpose, a five month experimental campaign is conducted which involves two wind tunnel tests and one fatigue test. The Ground Vibration Test GVT of the wing is performed using the fatigue test assembly.

5.1. Wind tunnel

The static and dynamic aeroelastic experiments are performed in the wind tunnel at the Delft University of Technology TU Delft. The wind tunnel is an Open Jet Facility OJF with an octagonal test section of 2.85 m × 2.85 m and has a maximum velocity of up to 35 m/s. The test setup consists of the gust generator, the manufactured composite wing and the measurement systems. Fig. 9 depicts the experimental setup along with the major components.

The gust generator is a device that produces unsteady flows in the form of sine and cosine gusts. The gusts are produced by two rectangular gust vanes with a symmetric NACA 0014 airfoil oscillating in pitch around an axis located at 23.7% of the its chord [29]. The gust vanes are supported by an aluminum frame and are placed in front of the outlet of the wind tunnel. The gusts produced by the gust generator have a maximum frequency of 10 Hz and maximum amplitude of 10 degrees. The gust vanes are controlled through the interface implemented in the National Instruments LABVIEW environment.The characteristics and the capabilities of the gust generator are described in more detail in [29].

The measurement systems used in the wind tunnel are the balance, scanning vibrometer and fiber optic sensing. All the measurement systems are synchronized with the gust generator using a trigger signal that is sent from the gust generator controller.

To measure the gust response, the gust loads are measured at the root of the wing with a six-component balance. The reference point of the balance is 168.5 mm below the mounting plate which needs to be accounted for while processing the wing root moments. Fig. 10 shows the axis system and the dimension of the balance. The wing is mounted on the balance through the wing mount and the balance is attached to the turn table. The turn table is a device which is used to change the angle of attack that the wing experiences by rotating the balance and wing setup. A splitter table is used to make sure there is clean airflow flowing over the wing.

The Polytec PSV-500 scanning vibrometer is used to measure the static and dynamic displacements of the composite wing. The polytec system is a single point non contact scanning vibration measurement system. With the vibrometer, ten points: five points each along the leading and the trailing edge of the wing, are monitored. Fig. 9 shows the location of the point on the wing.

The LUNA ODiSI-B, which is a fully distributed strain measurement system with up to 1.28 mm spatial resolution, is used as fiber optic sensing system. The ODiSI system uses a Optical Frequency Domain Reflectometer OFDR, which is used to analyze the local backscatter light intensity. The optical fiber from the wing is connected to the LUNA ODiSI-B through the OFDR. With this system, the spatial resolution for strain acquisition depends on the acquisition frequency: the higher the acquisition frequency the lower the spatial resolution. For the current experiments, the strain data is acquired every 5 mm with an acquisition rate of 100 Hz.

5.2. Fatigue test

To perform a realistic fatigue test of the composite wing, a distributed load equivalent to the aerodynamic load wing encounters during flight needs to be applied. For this purpose, a whiffle tree is

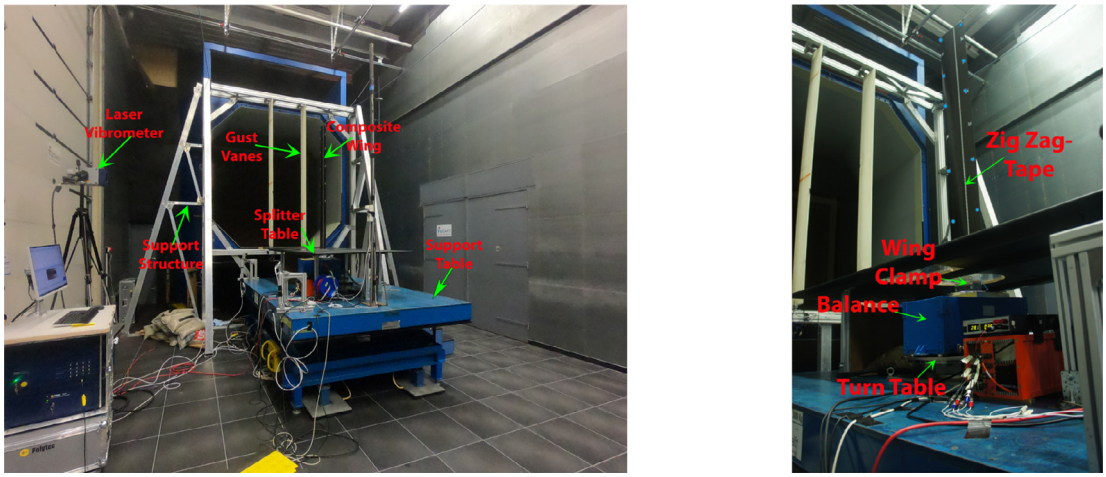

Fig. 9. Wind tunnel setup (blue dots represent the points monitored by the vibrometer).

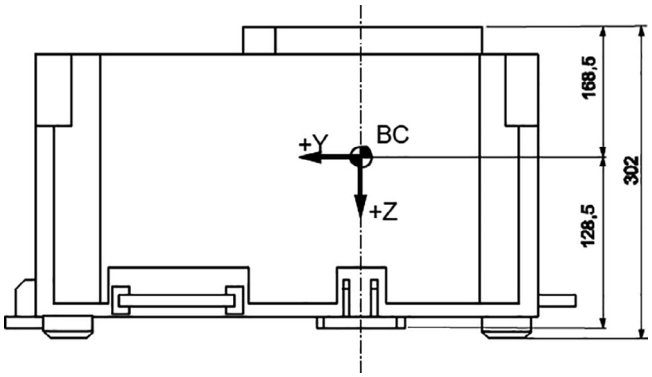

Fig. 10. Balance axis system and dimension (all the dimensions are in mm).

designed and manufactured to distribute the single actuator load from the fatigue machine into several discrete loads on the wing, thus approximating the distributed load on the wing. The discrete loads are applied through a cradle which is a wooden pad with a rubber lining.

The whiffle tree is designed and optimized to match the spanwise distribution of shear force, bending moment and torque obtained from PROTEUS for the first load case described in Table 5. This is also the cruise load case. The distributed loads are assumed to scale linearly with the load-factor. Thus all load shapes can be extrapolated from the 1G cruise shape. The design variables for the whiffle tree are as follows.

- The number of cradles.
- The fraction of the total load taken by each cradle.
- The spanwise location of each cradle.
- The chordwise location at which the load was introduced in all cradles.

It follows that, for a whiffle tree with N cradles, $2N + 1$ optimization variables will be present. The cradles are modelled as point loads and a gradient based optimizer is used to find an optimal design. Since it is possible to generate a different optimal design for each unique number of cradles, several optimal designs are analyzed. Using less than four cradles results in too large of an error between the target distributions obtained by PROTEUS and the load distributions achieved by the whiffle tree. Using more than six cradles only gave very marginal improvements. Fig. 11 shows the percentage error for the first

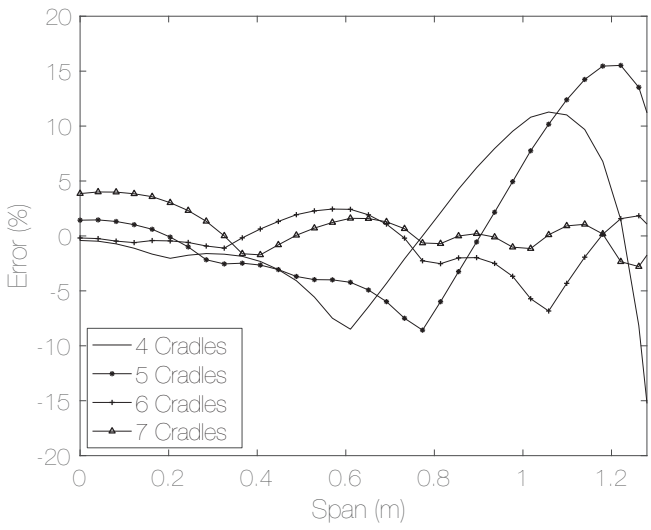

Fig. 11. Percentage error between the bending moment distribution achieved with different number of cradles in the whiffle tree and the target distribution obtained by PROTEUS.

1.2 meters of the wing between the bending moment distribution achieved with different number of cradles in the whiffle tree and the target distribution obtained by PROTEUS. Thus, the design with six cradles is selected for manufacturing the whiffle tree.

Table 7 shows the details of the whiffle tree design and Fig. 12 shows the sketch of the assembled whiffle tree. Fig. 13 compares the spanwise distributions of the shear force, torsion and bending moment induced by the whiffle tree compared to the target distribution obtained by PROTEUS. As can be seen, there is a good match with

Table 7
Summary of the final whiffle tree.

Cradle number	Spanwise location (%)	Fraction of total load (%)	Fraction assigned to front spar (%)
1	13.71	20.65	96.31
2	26.86	21.8	96.31
3	48	17.96	96.31
4	61.71	14.27	96.31
5	78.29	19.2	96.31
6	94.73	6.12	96.31

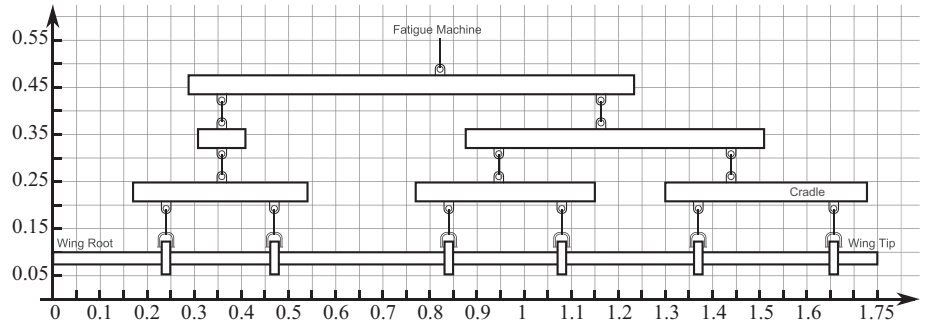

Fig. 12. Sketch of the whiffle tree setup (dimensions of the axes are in m).

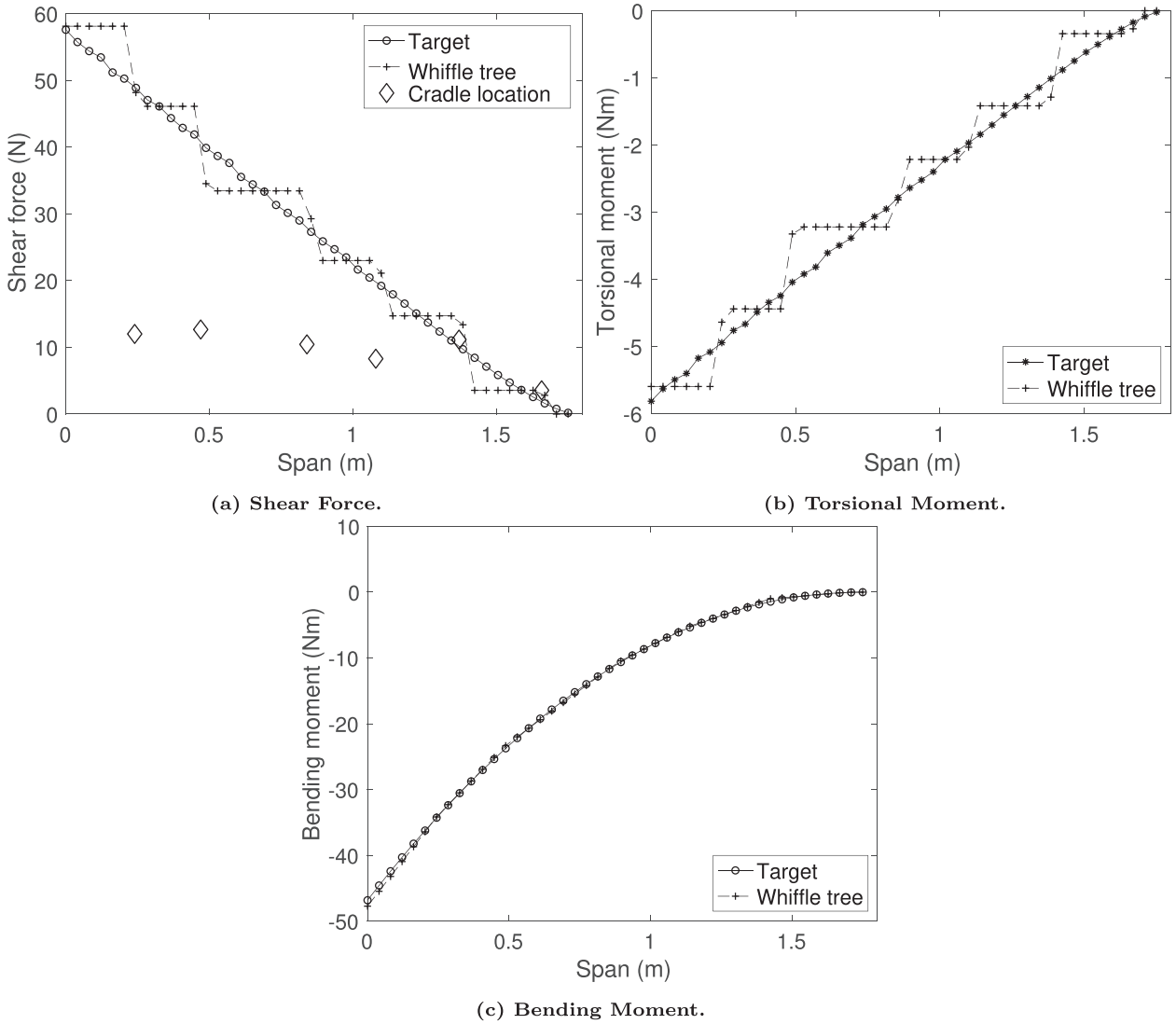

(a) Shear Force.

(b) Torsional Moment.

(c) Bending Moment.

Fig. 13. Spanwise distributions of the shear force, torsion and bending moment induced by the whiffle tree compared to the target.

shear force with maximum error less than 10% and an excellent match with the bending moment where the maximum error is less than 2%. The error with torsional moment is on the higher side with maximum error around 20%. The main reason for a higher error is the design choice that the load distribution between front and rear spar is the same for all the cradles. This design choice is made for the ease of manufacturing. If the load distribution is tailored for each separate cradle, then the match with the torsion could be improved. As the torsional loads applied by the whiffle tree are lower than the target loads and the angle of rotation of the wing is negligible, the error of 20% is deemed to be acceptable.

The whiffle tree is assembled using the spreader bars which are fashioned out of slotted aluminum beams, with a 40 mm by 40 mm cross section. The links between bars are created using carabiner hooks

connected to a pair of *M*8 lifting eye bolts (one on each beam). The lifting eye bolts are in turn connected to the beams by means of a T-slot nut that fits in a grove running along the beam's length. The bottom bars are linked to the cradles by means of a carabiner, which is in turn attached to a D-shackle running through the cradle's thickness. The master beam is connected to the actuator of the fatigue machine by means of a lifting eye bolt and a pin. Cradles are fashioned out of 18 mm thick plywood. The majority of these components can be seen in Fig. 14. Table 8 gives information on the materials of the components used to manufacture whiffle tree.

For each whiffle tree component, it was ensured that fatigue failure would never occur over the entire span of testing. If fatigue data for the particular component or material was available, it was ensured that the most critical load-case would be below the said endurance limit. If no fatigue data was available, it was ensured that the most critical load case would always be at least 10 times smaller than the static failure load.

The machine used for the fatigue testing of the composite wing is the MTS 100 kN fatigue machine. The machine has a maximum speed of 141 mm/s and a maximum displacement of 200 mm. Fig. 14 depicts the composite wing mounted in the fatigue setup. The wing is clamped onto the blue steel frame which supports the wing and connects it to the fatigue machine. An external load cell was connected between the machine and the wing through the whiffle tree. To measure the displacement of the wing, a Micro Epsilon laser sensor with a maximum range of 100 mm is mounted on the fatigue machine located at a distance of 650 mm along the span from the wing root.

5.3. Ground vibration test

To identify the natural frequencies of the composite wing, a GVT is performed on the wing in the clamped condition when it is attached to the blue steel frame for the fatigue testing. Fig. 15 displays the setup of the wing during the GVT.

A rowing hammer method is used to perform the GVT. Eighteen excitation points are chosen with 10 points on the wing itself and the remaining eight points on the supporting structure. The response is measured at two locations along the wing: at 75% wing span and at the tip of the wing. At each of these locations, there are two accelerometers; one measuring the in-plane response and another measuring the out-of-plane response. The responses are recorded through a National Instruments data card in the LABVIEW [30] environment. Simcenter Testlab [31] is then used to analyze the response and calculate the modal frequencies of the structure.

Table 8
Details of the components used to build the whiffle tree.

Component	Manufacturer	Material
Slotted aluminum beams	Item24	Aluminum 6060 alloy
Lifting eye bolts	Fabory	Stainless Steel
Nuts and Bolts	Fabory	Stainless Steel
Carabiners	Seilflechter	Stainless Steel
D-shackles	Toolstation	Galvanized Steel
Cradles	Gamma	Plywood

6. Results

As mentioned before, the experimental campaign consisted of two wind tunnel tests and one fatigue test. The first wind tunnel test aims at validating the static and dynamic aeroelastic model from PROTEUS and benchmarking the performance of the pristine wing. With the fatigue test, the objective is to validate the fatigue life prediction of the developed analytical fatigue model in PROTEUS. Finally, the aim of the second wind tunnel test is to understand the effect of fatigue on the aeroelastic response of the wing. Before presenting the discussion on the wind tunnel tests, the results from the GVT on the structural dynamic characterization of the composite wing is presented below.

6.1. Ground vibration test results

Table 9 depicts the measured experimental natural frequency and the calculated natural frequency of the PROTEUS model. As can be seen, except the second and third bending mode, all the other modes differ by more than 10%. The predictions for the second and third bending are relatively better with an error of around 3%. There are three main reasons for the discrepancy in the natural frequencies. First is the distribution of the masses. In the numerical model of PROTEUS, the LE strip is not modeled. Also, the added weight of the bond line and the four accelerometers are not modeled. This would lead to a different mass configuration, which could impact the natural frequencies. Second is the presence of the bond line and spar flanges, which affects the stiffness of the structure resulting in an effect on the natural frequencies. Both bond line and spar flanges are not modeled in PROTEUS. Finally, in the numerical model, a perfectly clamped boundary condition is used to evaluate the natural frequency, whereas, during the experiments, it is theoretically impossible to obtain a perfectly clamped wing. The clamping mechanism was made out of Aluminum which, because of lower stiffness compared to a material like steel, would induce some flexibility, affecting the natural frequencies.

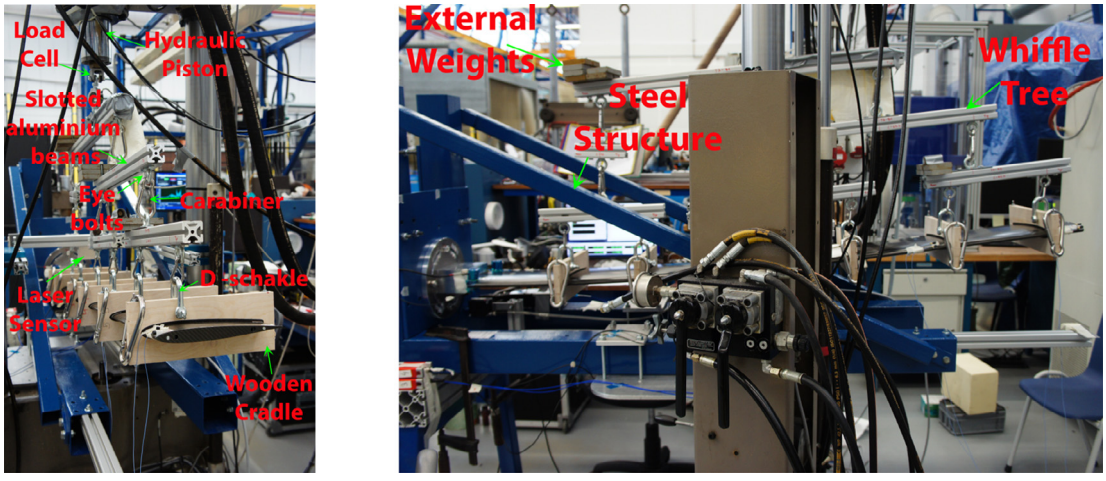

Fig. 14. Fatigue test setup.

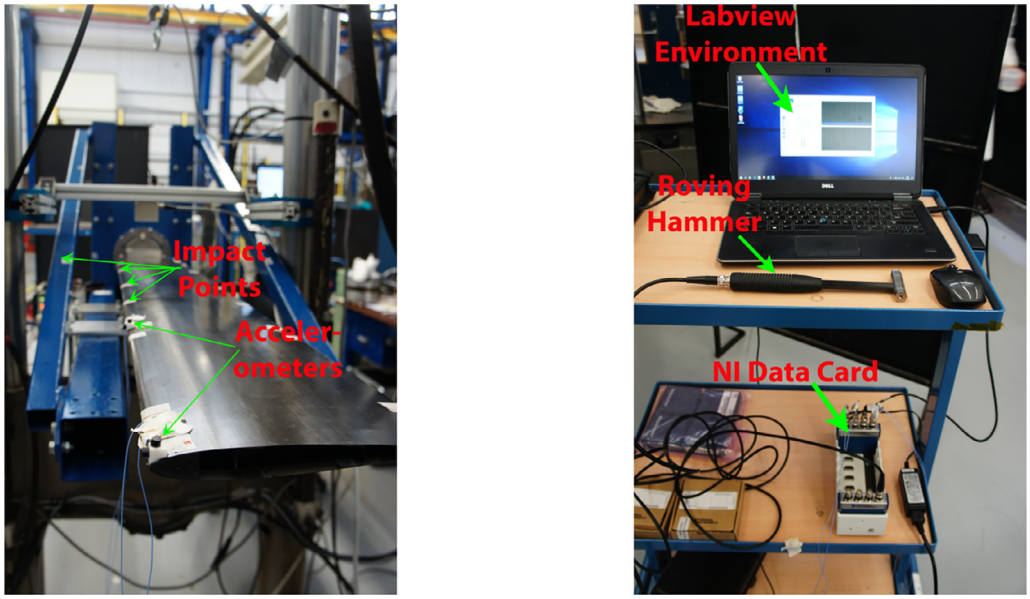

Fig. 15. GVT setup.

Table 9
Comparing natural frequency of the wing obtained experimentally with original PROTEUS model.

Mode No.	Mode description	Experiments (Hz)	PROTEUS (Hz)	Difference (%)
1	First Bending	5.40	6	11.1
2	Second Bending	25.99	26.39	1.9
3	First Inplane Bending	43.21	50.91	17.8
4	Third Bending	67.55	68.97	2.1
5	First Torsion	120	131.75	9.7
6	First Bending and Torsion	133.26	144.82	8.7

The PROTEUS model is modified by modeling the LE strip and taking into account the weights of the accelerometers. Table 10 shows the comparison of the experimental results and the modified PROTEUS model. As can be seen, except for the first in-plane bending mode, all the other modes have an error of less than 5.5%. The frequency of the first in-plane bending mode is approximately 9 times the frequency of the first bending mode and hence it will not have much influence over the aeroelastic response of the wing. Thus the current modified PROTEUS model is deemed to be sufficient for the objectives of the current experimental tests and hence, no further stiffness update is carried out on the PROTEUS model.

6.2. First wind tunnel test

In the wind tunnel test, both static and dynamic tests have been performed on the pristine wing. The test matrix for these tests is shown in Table 11. The aim of the first wind tunnel test is to compare the experimental results from static polar and gust envelope with the numerical results obtained from PROTEUS in order to validate the tool. Also, the results are used to benchmark the performance of the pristine wing.

Table 11
Test matrix for the wind tunnel tests.

	Static tests	Dynamic tests
Wind Velocity (m/s)	14,26	14,26
Static Angle of Attack (degrees)	−1,2,4,6,8,10	4
Gust frequency (Hz)	(–)	2,4,8
Gust amplitude (degrees)	(–)	5,10

As can be seen in Fig. 9, the wing is equipped with zig-zag tapes on pressure and suction side of the wing in order to force boundary layer transition from laminar to turbulent and, in this way, suppress any potential laminar separation bubble. A tape of 0.2 mm is applied on the suction side at 5% of the chord and a tape of 0.5 mm is applied on the pressure side at 65% of the chord. These values are selected according to the method presented by Braslow and Knox [32] and using airfoil pressure distributions predicted by XFoil [33].

Table 10
Comparing natural frequency of the wing obtained experimentally with modified PROTEUS model.

Mode No.	Mode Description	Experiments (Hz)	Modified PROTEUS (Hz)	Difference (%)
1	First Bending	5.40	5.66	4.8
2	Second Bending	25.99	25.93	-0.2
3	First Inplane Bending	43.21	49.47	14.4
4	Third Bending	67.55	66.24	−1.9
5	First Torsion	120	126.66	5.5
6	First Bending and Torsion	133.26	136.11	2.1

6.2.1. Static experiments

Fig. 16 depicts the lift coefficient of the wing for various angles of attack at a velocity of 26 m/s. With a mean error of around 8%, there is a reasonable agreement between PROTEUS and the experimental results with PROTEUS slightly over predicting the lift curve slope. One possible reason for the over prediction of the lift coefficient is the application of the zig-zag tape. The zig-zag tape causes the forced transition of the flow from laminar to turbulent and this effect is not captured by PROTEUS as the aerodynamic solver is based on the inviscid Vortex Lattice Method VLM. To understand the effect of zig-zag tape on the lift coefficient, a viscous and an inviscid analysis of the NACA 0010 airfoil is carried out using XFoil [33]. For the viscous analysis, forced transition at 5% and 65% of the chord on the top and bottom skin of the airfoil is applied, respectively. Fig. 17 compares the lift coefficient obtained with viscous and inviscid analysis. As can be seen, there is a mean error of around 10% between the two analyses for a 2D airfoil. This contributes to the overprediction of the lift coefficient by PROTEUS compared to the experimental results. Fig. 18 depicts the root bending moment coefficient of the wing for various angles of attack at a velocity of 26 m/s. There is an excellent agreement between PROTEUS and experimental results with an average error of less than 1%.

Fig. 19 compares the maximum longitudinal normal strain (axial strain) on the bottom skin measured using the optical fiber to the predictions from the PROTEUS. As can be seen, there is a good agreement with an error of less than 3%. The maximum strain occurs at 0.58 m from the root where the first laminate transitions into the second laminate with a ply drop of 4 plies. Fig. 20 plots the longitudinal normal strain (axial strain) distribution along the span of the bottom skin. There is a good match for the strains predicted from the PROTEUS and the experimental results at a lower angle of attack as the error at the peak strain is less than 0.5%. As the angle of attack increases, the error between the peak numerical and the experimental strain increases to 5.5%. This is due to the fact that as the angle of attack increases, the difference between the lift predicted by PROTEUS and experiments increases, which leads to a difference in the deformation of the wing leading to a higher difference in the strain experienced by the wing.

6.2.2. Dynamic experiments

For the dynamic measurements, the support table that can be seen in the wind tunnel setup depicted in Fig. 9 has the first eigenmode at around 5 Hz. Since the first bending mode of the wing is also at 5.4 Hz,

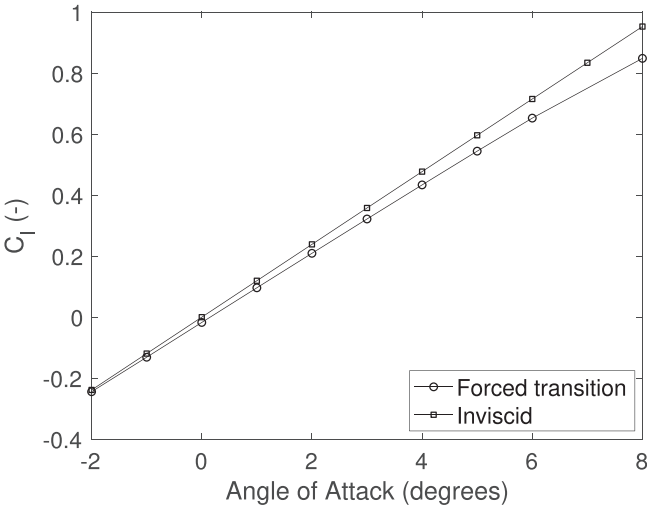

Fig. 17. Comparison of the 2D lift coefficient between viscous and inviscid solver.

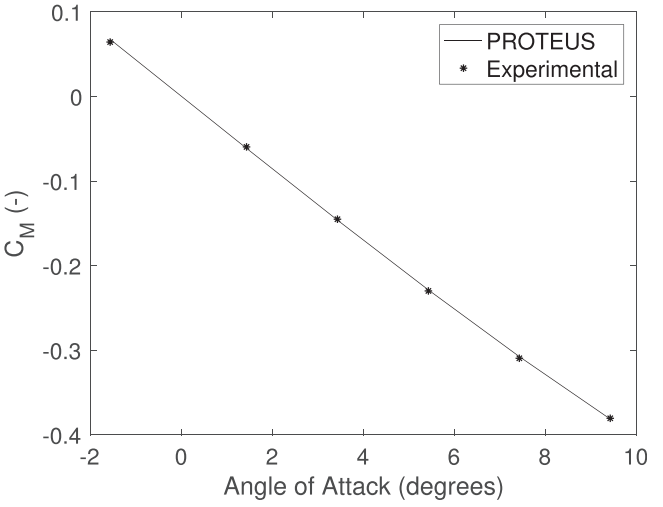

Fig. 18. Comparison of the root bending moment coefficient of the wing measured experimentally and numerically.

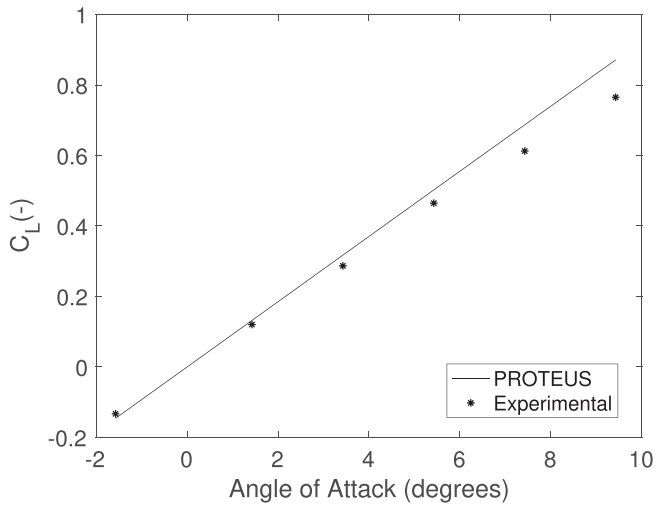

Fig. 16. Comparison of the lift coefficient of the wing measured experimentally with calculated numerically.

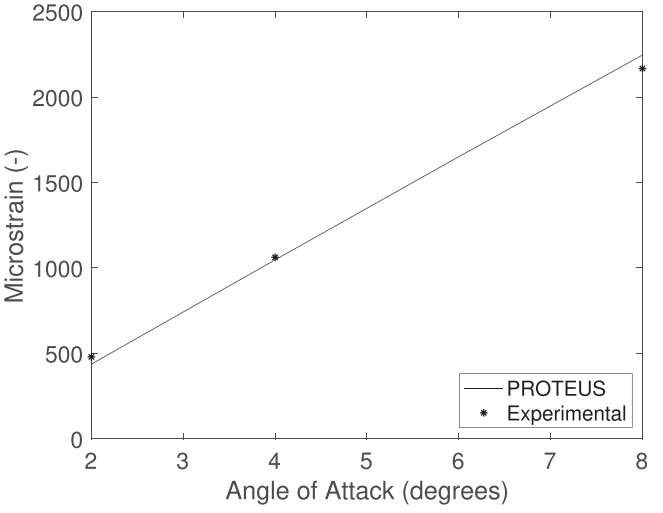

Fig. 19. Comparison of the maximum longitudinal normal strain (axial strain) measured numerically and experimentally.

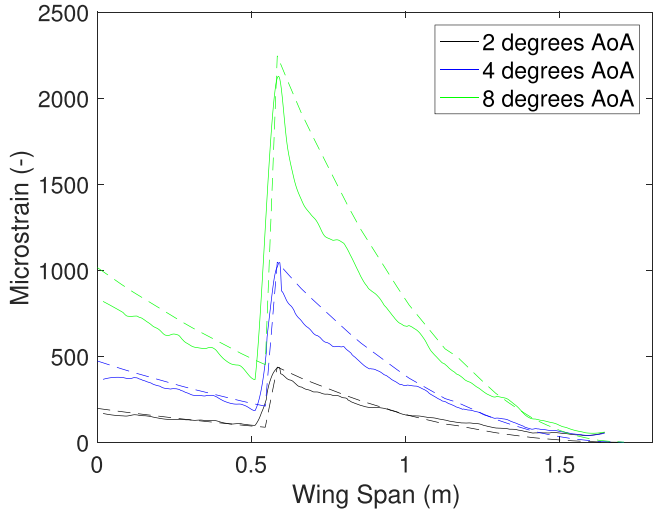

Fig. 20. Comparison of the longitudinal normal strain (axial strain) along the span measured numerically and experimentally ((– –) PROTEUS and (-) Experimental).

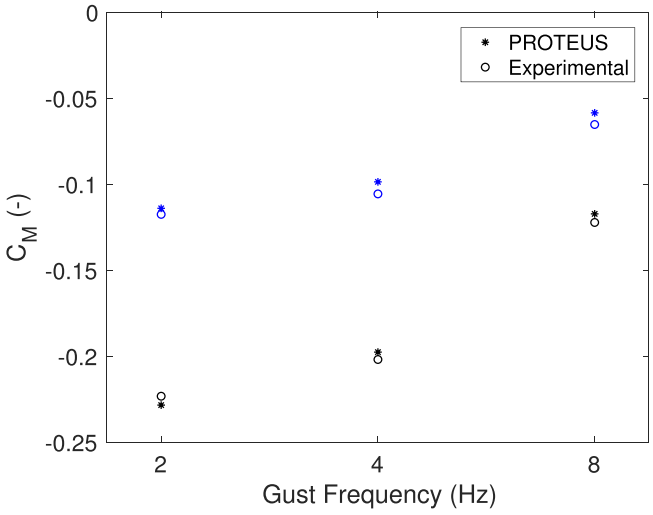

Fig. 22. Maximum dynamic root bending moment coefficient measured at different gust frequency and amplitude (Blue: 5 degrees gust amplitude, Black: 10 degrees gust amplitude).

the gust response of the wing is influenced by the dynamics of the support table. In an effort to clearly separate the eigenfrequency of the support table and the wing, the wing is fitted with a tip mass of 400 g, which reduces the first bending frequency of the wing from 5.4 Hz to 3.3 Hz.

From here on, all the dynamic results presented will be of the wing fitted with the tip mass. Moreover, only the incremental results due to the gust are considered in the current comparison.

Figs. 21 and 22 depict the maximum lift and root bending moment coefficients measured experimentally and calculated numerically at different gust frequencies and gust amplitudes for a velocity of 26 m/s. For the numerical prediction, a gust speed correction factor of 0.48 is applied to account for a decrease in the gust amplitude experienced by the wing [29]. As can be seen, there is a reasonable match between experimental and numerical predictions with a maximum error of around 10%. The error in the prediction can be attributed to the effect of zig-zag tape and the uncertainty in the gust speed correction factor. In general, the gust speed correction factor depends on the distance of the wing from the gust generator, the speed of the wind tunnel and the frequency of the gust. A small change in either of these factors could lead to a different correction factor. Based on the data available in [29], a constant correction factor of 0.48 can be reliably estimated. Encouragingly, the trends predicted by PROTEUS for the maximum lift and root bending moment coefficient follow the experimental evidence with the critical gust having a frequency of 2 Hz.

Fig. 23 compares the maximum tip deflection obtained numerically and experimentally at different gust frequencies and amplitudes and velocities. There is a good match for the tip displacements between the PROTEUS and experimental results with a maximum error of less than 10% except for the two measurement points, which have a frequency of 2 Hz and 4 Hz, gust amplitude of 10 degrees and velocity of 26 m/s. For these two measurement points, the error was due to the scanning vibrometer acquisition system not being able to capture

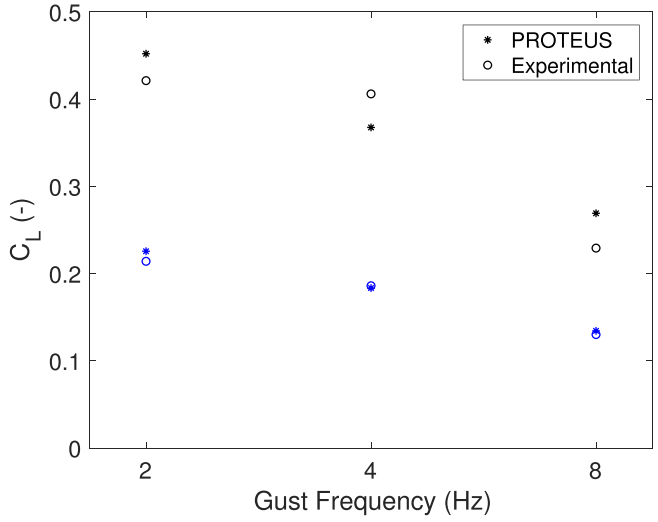

Fig. 21. Maximum dynamic lift coefficient measured at different gust frequency and amplitude (Blue: 5 degrees gust amplitude, Black: 10 degrees gust amplitude).

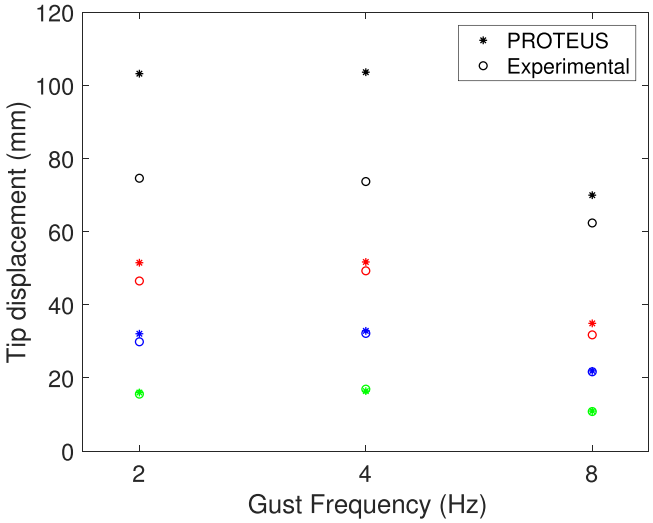

Fig. 23. Maximum tip displacement measured at different gust frequency, amplitude and velocity (Black: 10 degrees gust amplitude and 26 m/s velocity, Blue: 10 degrees gust amplitude and 14 m/s velocity, Red: 5 degrees gust amplitude and 26 m/s velocity,Green: 5 degrees gust amplitude and 14 m/s velocity). (For interpretation of the references to color in this figure legend, the reader is referred to the web version of this article.)

the large tip displacement at those points. Figs. 24 and 25 compare the time history of the tip displacement for a gust frequency of 4 Hz and 8 Hz having a velocity of 26 m/s and gust amplitude of 10 degrees. As can be seen, with a gust frequency of 8 Hz, the numerical tip displacement follows the experimental result quite well. However, for the 4 Hz gust, even though the frequency of the numerical response is in sync with the experimental response, the peak displacement is 30% higher than the experimental result. To measure the tip displacement, the laser from the scanning vibrometer is placed very close to the tip. At high out of plane displacement, the wingtip is out of the field of view of the laser and as a result, there is a loss of information which results in a flat line, as can be seen in Fig. 24. Nevertheless, if one follows the curvature of the response, the experimental tip displacement would be close to the numerical tip displacement.

Looking at the results from the first wind tunnel test, it can be concluded that PROTEUS predicts the static and gust responses of a composite wing with reasonable accuracy. This gives confidence in the tool to be used as a preliminary aeroelastic design tool for composite wing studies. Additionally, with these results, the static and dynamic performance of the pristine wing has been benchmarked and will be used later to compare the effect of fatigue on the aeroelastic response of the wing.

6.3. Fatigue results

After the first wind tunnel campaign, the wing is installed in the fatigue test machine, as shown in Fig. 14. The wing is subjected to a load controlled fatigue spectrum. The machine is set up in such a way that the spectrum is applied at a constant load rate rather than constant frequency. Constant load rate is preferred option due to ease in stability and controllability of the specimen. The rate of load applied is set at 60 N/s. With this applied load, a minimum frequency of 0.17 Hz and a maximum frequency of 0.65 Hz is achieved throughout the spectrum. It takes roughly one day to apply one block of $10,000$ cycles. As a result, roughly ten days are required to apply the design life of $100,000$ cycles. As mentioned before, the applied load and the displacement at 0.65 m from the root are continuously recorded. Additionally, at certain time intervals, the fatigue process is paused and a static load of 118 N is applied. The load of 118 N is twice the cruise load. At this load, the strains from the optical fiber and the tip displacement are recorded. The displacement at the point, which is 0.65 m from the root, will be referred to from here on as the mid-span displacement for the sake of brevity.

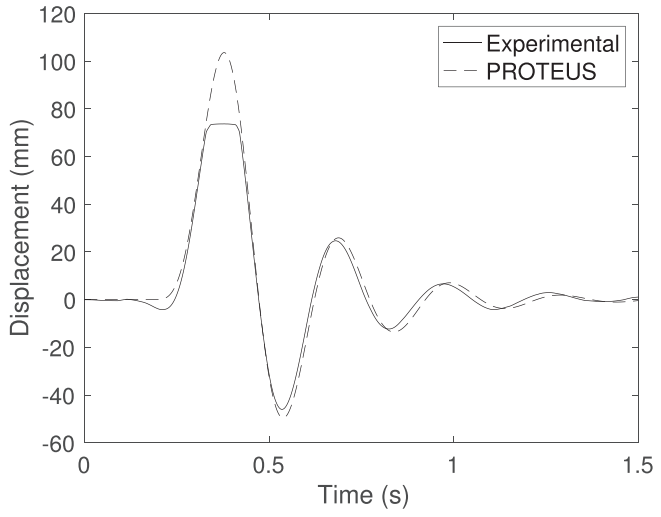

Fig. 24. Time history of tip displacement for a gust having a frequency of 4 Hz, amplitude of 10 degrees and velocity of 26 m/s.

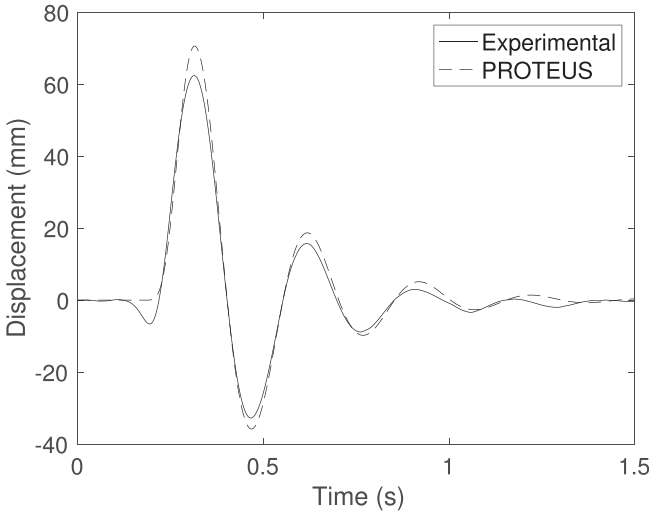

Fig. 25. Time history of tip displacement for a gust having a frequency of 8 Hz, amplitude of 10 degrees and velocity of 26 m/s.

Fig. 26 depicts the displacement of the tip measured at the specific interval during the fatigue life. As can be seen, there is approximately 9% increase in the tip deflection at an applied static load of 118 N over the 100,000 cycles. Fig. 27 depicts the mid-span displacement over the design life. The mid-span displacement is also increased by approximately 10%. As the mid-span displacement is recorded continuously at different load levels along the spectrum, in the current figure, the mid-span displacement of every 100 cycles is interpolated to find the mid-span displacement at 118 N. This assumes that the change in deflection over 100 cycles is negligible compared to the gradual change occurring over the 100,000 cycle duration. This leads to 1000 data points compared to 22 data points for the tip displacement. The gap in Fig. 27 relates to the error in the data recorded by the fatigue test machine for the respective cycles.

The reason for the increase in deflection can be attributed to a combination of reasons: relaxation of the test fixture, settling of the specimen and adhesive bond-lines, and stiffness degradation due to multi-scale damage creation and evolution. For a composite material, a stiffness degradation over a fatigue life consists of three stages [34]. In stage 1, there is a steep drop in stiffness due to initial defect in the structure and material relaxation, in stage 2, there is gradual degrada-

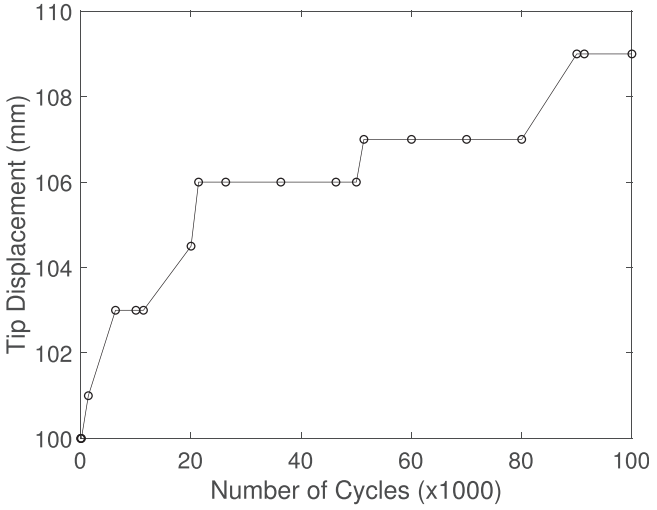

Fig. 26. Maximum tip displacement with respect to number of cycles.

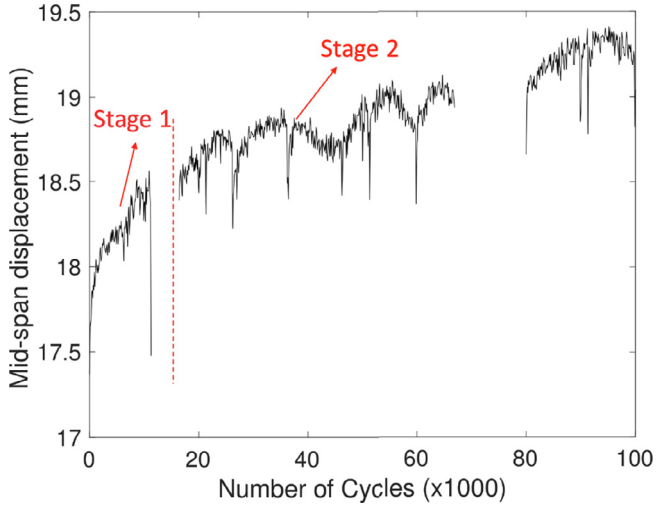

Fig. 27. Mid-span displacement with respect to number of cycles.

tion in stiffness due to the development of delamination and matrix cracking and finally in stage 3, there is sudden degradation in stiffness because of the fatigue induced fiber breakage leading to final failure. A similar kind of behavior is seen in Fig. 27, where there is an initial increase in the deflection until 20,000 cycles, after which the increase in the displacement becomes more gradual until 100,000 cycles. The tip deflection curve looks discontinuous with a prolonged period of constant stiffness and a short period of stiffness drops. This is due to the fact that tip displacement is measured manually with an accuracy of 1 mm and at specific intervals. A behavior similar to mid-span displacement would be observed with a continuous recording of the tip displacement over the fatigue life.

Fig. 28 displays the change in the maximum normal and shear strain experienced by the bottom skin with respect to the number of cycles. The maximum strains occur at the ply drop, as was the case in the wind tunnel test. The points in the figure display the experimental values captured by the optical fiber. Since the data is noisy due to the sensitivity of the optical fiber, a trend line calculated using least square method, indicated by a solid line helps to understand the pattern of the strain with respect to the number of cycles. There is an increase of 20 microstrains (10%) in shear, whereas the transverse normal strain increases by 30 microstrains (8%) over 100,000 cycles. The maximum increase is observed in the axial strain, which increases by approximately 230 microstrains (10%). This change is partly due to the degradation in axial stiffness of the laminate. This degradation leads to higher deflection as can be seen in Figs. 26 and 27.

Fig. 29 displays the longitudinal normal stain (axial strain) along the wingspan at different cycles. As is mentioned before, the maximum strain occurs at ply drop and the maximum strain increases as the number of cycles increases. An interesting observation that can be made is that, as the number of cycles increases, the axial strain increases across the entire wingspan except at the outer part of the wing. This is due to the load redistribution because of the stiffness degradation. As the wing fatigues, the reduced stiffness in the outer part attracts lower loads, resulting in lower strains.

Traditionally, a composite wing, designed with a fatigue knockdown factor of 0.32 on the maximum stress allowables, will not experience strains high enough to cause stiffness degradation of the magnitude measured here. Since the current wings are designed using the analytical fatigue model instead of the knockdown factor, higher strains are experienced by the wing, which leads to an increased degradation in stiffness. The analytical model [11] is based on the residual strength and does not model the degradation in stiffness. Thus, numerically, the wing is optimized in such a way that the wing will have sufficient residual strength until 100,000 cycles to carry the critical loads. With the experiments, after 100,000 cycles, the fatigued wing is tested again in the wind tunnel as explained in the following section. The wing is able to withstand critical static and gust loads. This proves that even though there was a drop in stiffness, there was no damage at a long enough scale to compromise strength leading to the wing having enough residual strength to carry the applied load. This validates the analytical fatigue model.

With the current methodology, the wing is designed for precisely 100,000 cycles. This means at the $100,001^{st}$ cycle, the wing will theoretically fail. Looking at Fig. 27, the wing is in the second stage of the fatigue degradation curve and since third phase is about 20% of fatigue life, this specific wing with the specific material batch used and fabrication method accuracy achieved is still a bit far from a failure after the design life of 100,000 cycles is completed. This points to the fact that the numerical model is conservative in nature and the wing is overdesigned. This conservativeness can be attributed to three phenomena. First is the fact that the fatigue model is implemented within the lamination parameter domain, which is inherently conservative due to the use of the modified Tsai Wu Failure criterion. The second reason is the use of the first ply failure criterion as the fatigue failure criterion of the wing. With this criterion, as soon as a single ply

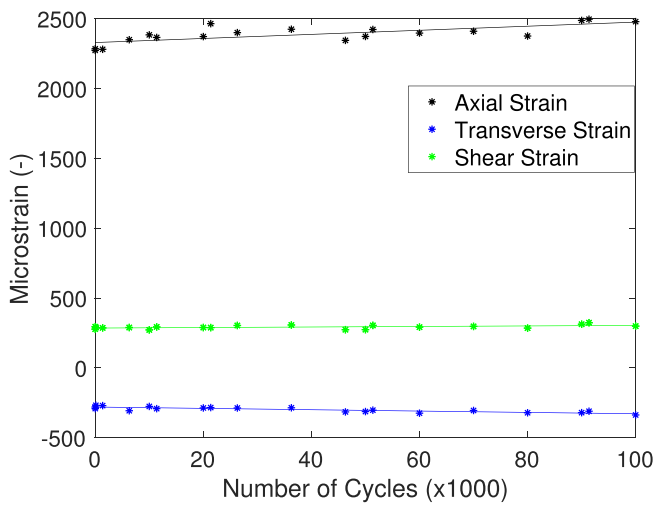

Fig. 28. Strain history with respect to number of cycles.

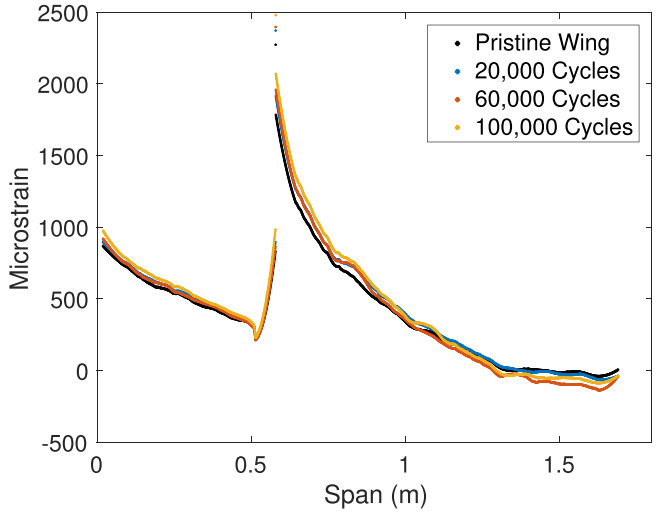

Fig. 29. Longitudinal normal strain (axial strain) along the span at different cycles.

locally fails, the wing is deemed to be failed in fatigue. Whereas in reality, even if there is some kind of damage in the ply, the wing as a whole has sufficient strength to carry the loads. Thirdly, the scatter is quite high in the fatigue of composite materials [35]. There is a possibility that this experiment is on the right side of the scatter, which would lead to a conservative result.

To understand how conservative the numerical model is, ideally, the wing would be fatigued until failure. Since in the current experimental campaign focus is also on the effect of the fatigue on the aeroelastic response of the wing, the wing is not fatigued further.

6.4. Second wind tunnel test

The fatigued wing is tested again in the wind tunnel with a setup similar to the one shown in Fig. 9. Both static and dynamic measurements are performed with the aim to compare the experimental response of the pristine wing with respect to the fatigued wing.

Fig. 30 shows the lift coefficient of the pristine and the fatigued wing for different angle of attack at a velocity of 26 m/s. The solid and the dashed line represent the linear fit of the experimental data for the pristine and the fatigued wing, respectively. As can be seen, the lift curve slope of the fatigued wing is 11% lower than that of the pristine wing. This reduction in the lift curve slope can be attributed to the degradation of the stiffness or to the experimental scatter that is caused due to variability in testing conditions. However, looking at Figs. 26 and 27, around 9% increase in the deflection of the wing, indicating degradation in stiffness, does point to the fact that reduction in the lift curve slope could be mainly due to degradation in the stiffness.

Due to the degradation in the stiffness, the fatigued wing will go to a higher deflection resulting in a more nose-down twist of the outboard part of the wing leading to reduced forces generated on the wing. This contributes to the lower lift curve slope.

Fig. 31 shows the force normalized axial strain along the wingspan for the velocity of 26 m/s at 4 degrees angle of attack. Force normalized axial strain is the axial strain normalized by applied force. Force normalized axial strain can be considered as an equivalent to static stiffness where, the higher the value of the force normalized strain, the lower is the stiffness. An approximate increase of 10% in the force normalized strain value agrees well with the increase of about 9% of the tip deflection seen during the fatigue tests.

Fig. 32 shows the maximum lift coefficient for a different combination of velocity, gust frequency and gust amplitude. A similar behavior

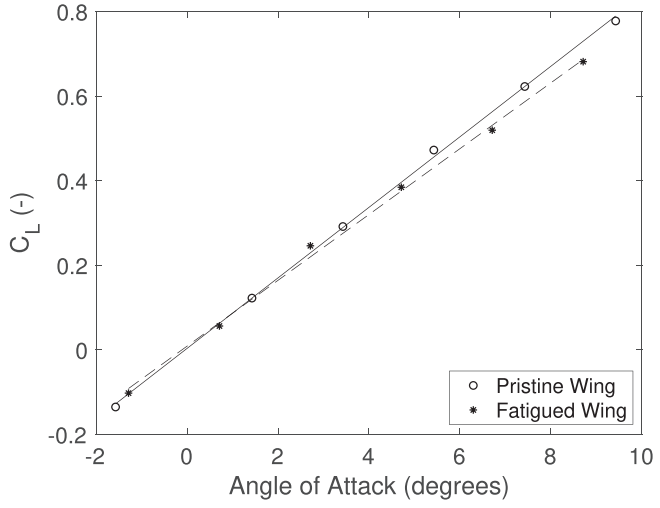

Fig. 30. Comparison of the lift coefficient of the pristine and the fatigued wing.

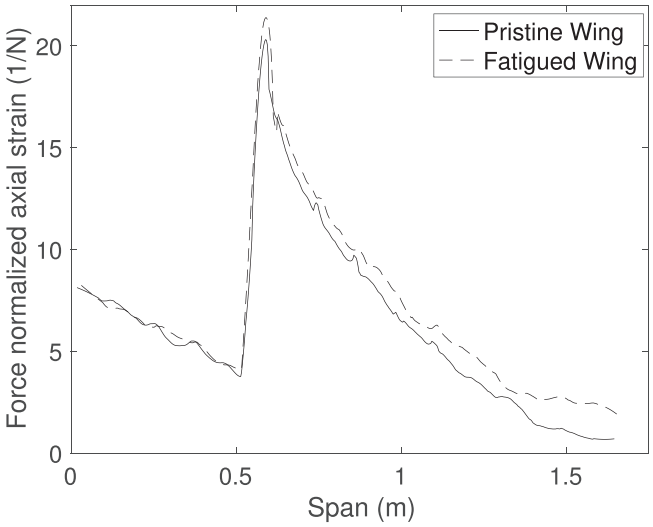

Fig. 31. Comparison of the force normalized normal strain along the wing span of the pristine and the fatigued wing.

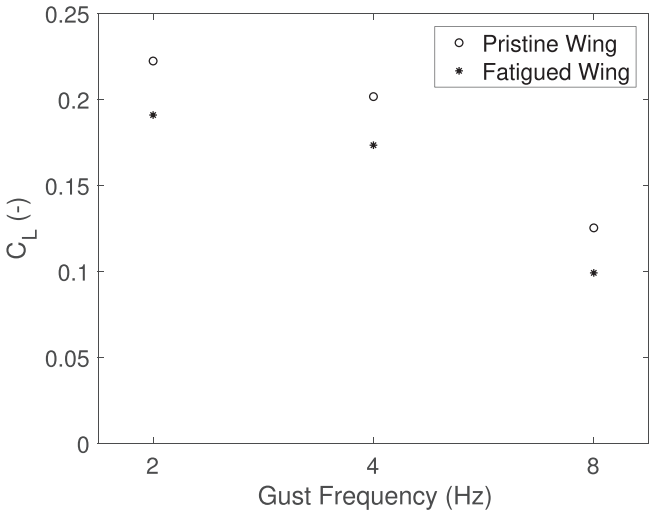

Fig. 32. Comparison of the maximum lift coefficient of the pristine and the fatigued wing for the gust amplitude of 5 *degrees*.

to the static condition is observed where the maximum lift coefficient for the fatigued wing is lower than the pristine wing by approximately 15%. The tip displacement of the pristine and the fatigued wing for a velocity of 26 m/s, frequency of 4 Hz and gust angle of 5 degrees is shown in Fig. 33. As explained earlier, a combination of lower stiffness and higher nose down twist lead to lower lift which, in turn, results in a lower tip displacement. Additionally, the frequency of the fatigued wing is also slightly lower (0.2 Hz) than the pristine wing. The reasons for such a small difference is that the first bending frequency is at 3.3 Hz. So even a 6–9% drop in stiffness will result in a small change in the first bending frequency.

Based on the results from the static and dynamic measurements, two main conclusions can be drawn. The first is that even after undergoing fatigue for 100,000 cycles, the wing is strong enough to withstand both static as well as gust loads. This again validates the numerical design methodology of accounting for fatigue through the analytical model instead of the knockdown factor. This, as demonstrated in [11] leads to lower weight designs. The second conclusion is that the aeroelastic response of the fatigued wing results in a lower lift coefficient for the same angle of attack compared to the pristine

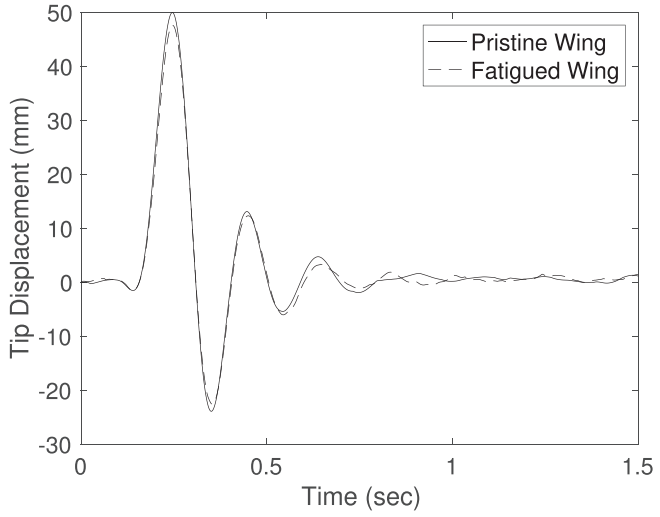

Fig. 33. Comparison of the tip displacement of the pristine and the fatigued wing for the gust amplitude of 5 *degrees*.

wing. The primary reason for the lower lift coefficient is the degradation in the stiffness caused by the fatigue process. This means that in order to attain a similar cruise lift coefficient, the trim angle of attack for the fatigued wing will be higher than the pristine wing. This would result in an increase in drag coefficient and hence, reduction in the lift to drag ratio leading to degradation in the performance due to an increase in fuel consumption.

In the traditional design of the composite wings, where the fatigue is accounted for by knocking down the stress allowables, the stresses are so low that there would not be any degradation in the stiffness properties of the wing leading to a negligible change in the aeroelastic response of the wing over the design life. This leads to wings being optimized for a single cruise point. With the design methodology proposed in the current research using the analytical model, the stresses in the wing would be higher during the fatigue process, which would lead to stiffness reduction over the life cycle of the aircraft. Even with the degraded stiffness, the wing will still have enough residual strength to carry the applied loads. However, the cruise condition of the wing will change over the design life and to obtain optimum performance over the entire design life, different cruise points need to be taken into account during the optimization of the wings.

7. Summary & conclusions

The aim of the paper was to validate the numerical design methodology for aeroelastic optimization of composite wings designed for gust and fatigue loads. Additionally, since the design methodology did not take into account stiffness degradation during fatigue, the goal was also to understand the effect of fatigue on the stiffness of the wing and, thus, on the aeroelastic response of the wing. For this purpose, a flexible composite wing with a span of 1.75 m and chord of 0.25 m was designed to be critical in strength, buckling and fatigue. For fatigue, a test spectrum load of 100,000 cycles was used as a design life. The optimized wing was manufactured using Hexply 1M7/8552 unidirectional UD prepreg.

An experimental campaign consisting of two wind tunnel tests and a fatigue test was conducted to meet the goals of the research. The results of the first wind tunnel campaign validated the aeroelastic part of the numerical design methodology as the experimental static and gust response of a composite wing matched the numerical predictions with reasonable accuracy with a maximum error of less than 8%. These results were also used to benchmark the static and gust performance of the pristine wing.

The wind tunnel test was then followed by a fatigue test, in which a whiffle tree was used to replicate a realistic load distribution on the wing. The wing was fatigued for 100,000 cycles using a spectrum based on the Mini-TWIST. The fatigue process resulted in the degradation of the stiffness, which led to an increase in tip deflection by 9% and in normal axial strain by around 10%. After 100,000 cycles, the wing did not experience any failure and had sufficient strength to withstand the critical load. This validated the analytical fatigue model; however, as the wing was not close to the failure, the analytical model could still be conservative in the fatigue prediction.

Finally, to check the effect of fatigue on the aeroelastic response of the wing, the fatigued wing was again mounted in the OJF and the static and dynamic experiments were once again performed. Comparing the performance of the fatigued wing with the pristine wing, the degradation in the lift curve slope was observed. As the stiffness degrades, the deflection of the wing increases for a given force leading to a more washout, which results in a lower lift. As a result, for a given angle of attack, the pristine wing will generate a higher lift force compared to the fatigued wing. This would lead to a higher cruise angle of attack for a fatigued wing leading to a higher drag coefficient and lower the lift to drag ratio and thus higher fuel consumption.

A wing designed traditionally by considering a knockdown factor for fatigue will result in a heavier wing, but with lower or no degradation in stiffness over its design life. A wing designed with the current methodology of taking into account fatigue through analytical model will result in the lighter wing but with degradation in stiffness over the design life. This degradation results in a change in the cruise angle of attack, which then also needs to be taken into account during the optimization process to avoid degradation in performance because of fatigue over the design life.

Declaration of Competing Interest

The authors declare that they have no known competing financial interests or personal relationships that could have appeared to influence the work reported in this paper.

References

[1] Eastep F, Tischler V, Venkayya V, Khot N. Aeroelastic tailoring of composite structures. J Aircraft 1999;36(6):1041–7.
[2] Arizono H, Isogai K. Application of genetic algorithm for aeroelastic tailoring of a cranked-arrow wing. J Aircraft 2005;42(2):493–9.
[3] Dillinger J, Klimmek T, Abdalla MM, Gürdal Z. Stiffness optimization of composite wings with aeroelastic constraints. J Aircraft 2013;50(4):1159–68.
[4] Guo S, Cheng W, Cui D. Aeroelastic tailoring of composite wing structures by laminate layup optimization. AIAA J 2006;44(12):3146–50.
[5] Stodieck O, Cooper JE, Weaver PM, Kealy P. Improved aeroelastic tailoring using tow-steered composites. Compos Struct 2013;106:703–15.
[6] Stanford BK, Jutte CV, Wieseman CD. Trim and structural optimization of subsonic transport wings using nonconventional aeroelastic tailoring. AIAA J 2015;54 (1):293–309.
[7] Jutte C, Stanford BK. Aeroelastic tailoring of transport aircraft wings: State-of-the-art and potential enabling technologies. NASA Tech. Rep. TM2014-218252(2014)..
[8] Rajpal D, Gillebaart E, Breuker RD. Preliminary aeroelastic design of composite wings subjected to critical gust loads. Aerosp Sci Technol 2019;85:96–112.
[9] Khodaparast HH, Georgiou G, Cooper JE, Riccobene L, Ricci S, Vio G, Denner P. Efficient worst case -1-cosine- gust loads prediction. J Aeroelast Struct Dyn 2012;2 (3).
[10] Werter NP, Sodja J, De Breuker R. Design and testing of aeroelastically tailored wings under maneuver loading. AIAA J 2016;55(3):1012–25.
[11] Rajpal D, Kassapoglou C, De Breuker R. Aeroelastic optimization of composite wings including fatigue loading requirements. Compos Struct 2019;111248.
[12] Sherrer V, Hertz T, Shirk M. Wind tunnel demonstration of aeroelastic tailoring applied to forward swept wings. J Aircraft 1981;18(11):976–83.
[13] Landsberger BJ, Dugundji J. Experimental aeroelastic behavior of unswept and forward-swept cantilever graphite/epoxy wings. J Aircraft 1985;22(8):679–86.
[14] Chen G-S, Dugundji J. Experimental aeroelastic behavior of forward-swept graphite/epoxy wings with rigid-body freedom. J Aircraft 1987;24(7):454–62.
[15] Meddaikar YM, Dillinger JK, Sodja J, Mai H, De Breuker R. Optimization, manufacturing and testing of a composite wing with maximized tip deflection. In: 57th AIAA/ASCE/AHS/ASC structures, structural dynamics, and materials conference; 2016. p. 0489..

[16] Meddaikar MY, Dillinger J, Ritter MR, Govers Y. Optimization & testing of aeroelastically-tailored forward swept wings. In: IFASD 2017-international forum on aeroelasticity and structural dynamics. p. 1–13.
[17] Ritter M, Dillinger J, Meddaikar YM. Static and dynamic aeroelastic validation of a flexible forward swept composite wing. In: 58th AIAA/ASCE/AHS/ASC structures, structural dynamics, and materials conference; 2017. p. 0637..
[18] Open Jet Facility. TU Delft, https://www.tudelft.nl/lr/organisatie/afdelingen/aerodynamics-wind-energy-flight-performance-and-propulsion/facilities/low-speed-wind-tunnels/open-jet-facility, [Visited on October 2019]..
[19] Macquart T. Optibless: An open-source toolbox for the optimisation of blended stacking sequence. In: ECCM17 – 17th European conference on composite materials, ECCM; 2016..
[20] MSCNastran. https://www.mscsoftware.com/product/msc-nastran, [Visited on August 2019]..
[21] Dillinger J. Static aeroelastic optimization of composite wings with variable stiffness laminates. Ph.D. thesis, Delft University of Technology; 2015..
[22] Kassapoglou C. Design and analysis of composite structures: with applications to aerospace structures. 2nd Ed., Aerospace Series, Wiley, John Wiley & Sons Ltd, The Atrium, Southern Gate, Chichester, West Sussex, PO19 8SQ, United Kingdom; 2013..
[23] Mitrotta FMA, Rajpal D, Sodja J, De Breuker R. Multi-fidelity design of an aeroelastically tailored composite wing for dynamic wind-tunnel testing. In: AIAA Scitech 2020 forum; 2020. p. 1636..
[24] Hammer VB, Bendsøe M, Lipton R, Pedersen P. Parametrization in laminate design for optimal compliance. Int J Solids Struct 1997;34(4):415–34.
[25] Raju G, Wu Z, Weaver P. On further developments of feasible region of lamination parameters for symmetric composite laminates. In: 55th AIAA/ASMe/ASCE/AHS/SC structures, structural dynamics, and materials conference; 2014. p. 1374..
[26] Wu Z, Raju G, Weaver PM. Framework for the buckling optimization of variable-angle tow composite plates. AIAA J 2015;53(12):3788–804.
[27] Khani A, IJsselmuiden ST, Abdalla MM, Gürdal Z. Design of variable stiffness panels for maximum strength using lamination parameters. Compos Part B Eng 2011;42(3):546–52..
[28] Lowak H, DeJonge J, Franz J, Schütz D. Minitwist - a shortened version of twist. NLR MP 79018 U 1979.
[29] Lancelot PM, Sodja J, Werter NP, De Breuker R. Design and testing of a low subsonic wind tunnel gust generator. Adv Aircraft Spacecr Sci 2017;4(2):125.
[30] Elliott C, Vijayakumar V, Zink W, Hansen R. National Instruments LabVIEW: A programming environment for laboratory automation and measurement. J Assoc Lab Automat 2007;12(1):17–24.
[31] Simcenter Testlab. https://www.plm.automation.siemens.com/global/en/products/simcenter/testlab.html, [Visited on August 2019]..
[32] Braslow AL, Knox EC. Simplified method for determination of critical height of distributed roughness particles for boundary-layer transition at mach numbers from 0 to 5. Tech. rep., Naca-tn-4363, National Advisory Committee for Aeronautics; 1958..
[33] Drela M. Xfoil: An analysis and design system for low reynolds number airfoils. In: Low Reynolds number aerodynamics. Springer; 1989. p. 1–12..
[34] Talreja R. Fatigue of composite materials; 1987..
[35] Tomblin J, Seneviratne W. Determining the fatigue life of composite aircraft structures using life and load-enhancement factors, Air Traffic Organization NextGen & Operations Planning Office of Research and Technology Development Washington, DC 20591; 2011..